

DEEP IMAGING OF THE HCG 95 FIELD. I. ULTRA-DIFFUSE GALAXIES

DONG DONG SHI,^{1,2} XIAN ZHONG ZHENG,^{1,2,3} HAI BIN ZHAO,^{1,4} ZHI ZHENG PAN,¹ BIN LI,^{1,4} HU ZOU,⁵ XU ZHOU,⁵
KEXIN GUO,⁶ FANG XIA AN,¹ AND YU BIN LI^{7,8,9}

¹Purple Mountain Observatory, Chinese Academy of Sciences, 2 West Beijing Road, Nanjing 210008, China

²School of Astronomy and Space Sciences, University of Science and Technology of China, Hefei 230026, China

³Chinese Academy of Science South America Center for Astronomy, China-Chile Joint Center for Astronomy, Camino El Observatorio #1515, Las Condes, Santiago, Chile

⁴Key Laboratory of Planetary Sciences, Chinese Academy of Sciences, 2 West Beijing Road, Nanjing 210008, China

⁵Key Laboratory of Optical Astronomy, National Astronomical Observatories, Chinese Academy of Sciences, Beijing 100012, China

⁶Kavli Institute for Astronomy and Astrophysics, Peking University, Beijing 100871, China

⁷Yunnan Observatories, Chinese Academy of Sciences, 396 Yangfangwang, Guandu District, Kunming 650216, China

⁸Center for Astronomical Mega-Science, Chinese Academy of Sciences, 20A Datun Road, Chaoyang District, Beijing 100012, China

⁹Key Laboratory for the Structure and Evolution of Celestial Objects, Chinese Academy of Sciences, 396 Yangfangwang, Guandu District, Kunming 650216, China

ABSTRACT

We present a detection of 89 candidates of ultra-diffuse galaxies (UDGs) in a 4.9 degree² field centered on the Hickson Compact Group 95 (HCG 95) using deep g - and r -band images taken with the Chinese Near Object Survey Telescope. This field contains one rich galaxy cluster (Abell 2588 at $z=0.199$) and two poor clusters (Pegasus I at $z=0.013$ and Pegasus II at $z=0.040$). The 89 candidates are likely associated with the two poor clusters, giving about 50 – 60 true UDGs with a half-light radius $r_e > 1.5$ kpc and a central surface brightness $\mu(g, 0) > 24.0$ mag arcsec⁻². Deep z' -band images are available for 84 of the 89 galaxies from the Dark Energy Camera Legacy Survey (DECaLS), confirming that these galaxies have an extremely low central surface brightness. Moreover, our UDG candidates are spread over a wide range in $g - r$ color, and $\sim 26\%$ are as blue as normal star-forming galaxies, which is suggestive of young UDGs that are still in formation. Interestingly, we find that one UDG linked with HCG 95 is a gas-rich galaxy with HI mass $1.1 \times 10^9 M_\odot$ detected by the Very Large Array, and has a stellar mass of $M_\star \sim 1.8 \times 10^8 M_\odot$. This indicates that UDGs at least partially overlap with the population of nearly dark galaxies found in deep HI surveys. Our results show that the high abundance of blue UDGs in the HCG 95 field is favored by the environment of poor galaxy clusters residing in HI-rich large-scale structures.

Keywords: galaxies: group: individual: (HCG 95) — galaxies: evolution — galaxies: structure

1. INTRODUCTION

Extremely low surface brightness (LSB) galaxies with unexpectedly large sizes, namely ultra-diffuse galaxies (UDGs), have recently drawn much attention to the understanding of their formation and evolution. Findings of dwarf galaxies with extreme LSB have been reported two decades ago (e.g., [Impey et al. 1988](#); [Bothun et al. 1991](#)). UDGs were detected in the Coma cluster using deep low-resolution imaging data obtained with small telescopes ([van Dokkum et al. 2015a](#)), and more UDGs were found in nearby galaxy clusters since then ([Koda et al. 2015](#); [Mihos et al. 2015](#); [Muñoz et al. 2015](#); [Beasley et al. 2016](#); [van der Burg et al. 2016](#); [Koch et al. 2017](#); [Román & Trujillo 2017a](#)). Differing from the classical LSB galaxies that usually have a central surface brightness down to $\mu(B, 0) \sim 22 - 23 \text{ mag arcsec}^{-2}$ ([Impey & Bothun 1997](#); [Impey et al. 2001](#); [Ceccarelli et al. 2012](#); [Geller et al. 2012](#)), UDGs have a much lower central surface brightness ($\mu(g, 0) = 24 - 26 \text{ mag arcsec}^{-2}$), but their half-light radius $r_e > 1.5 \text{ kpc}$ is comparable to that of typical L^* galaxies, and their stellar mass ($< \sim 10^8 M_\odot$) is two orders of magnitude lower ([van Dokkum et al. 2015a](#)). They usually appear to be red, relatively round, and morphologically featureless in galaxy clusters, but are blue and irregular in the field ([Merritt et al. 2016](#); [Leisman et al. 2017](#); [Román & Trujillo 2017a,b](#); [Trujillo et al. 2017](#)). The ultra-diffuse nature of UDGs remains little explored.

Increasing effort has been made to understand the formation of UDGs and their connections with other galaxy populations. However, the observations have so far led to diverse conclusions. Measurements of velocity dispersion of some UDGs (e.g., Dragonfly 44 in Coma) suggest that they are likely to be failed L^* galaxies that are overwhelmingly dominated by dark matter, although the reasons for their extremely low star formation efficiency in the past are still unknown ([van Dokkum et al. 2016](#)). Recently, [van Dokkum et al. \(2017\)](#) reported that the halo masses of largest Coma UDGs (Dragonfly 44 and Dragonfly X1) are at the level of $\sim 5 \times 10^{11} M_\odot$, lower than the previous estimate. The evidence of a high abundance of globular clusters in UDG Dragonfly 17 supports that it could be a failed galaxy with a halo mass similar to the halo masses of the Large Magellanic Cloud (LMC) or M33 ([Beasley & Trujillo 2016](#); [Peng & Lim 2016](#)). Additionally, VCC 1287, a UDG that is found in the Virgo cluster and with a halo mass estimated from the kinematics of globular clusters, is thought to belong to the dwarf galaxy population, although it is rather extended ($r_e = 2.4 \text{ kpc}$) ([Beasley et al. 2016](#)). More observations for a large sample of UDGs are thus needed to study the properties of UDGs in detail.

From the theoretical perspective, [Amorisco et al. \(2016\)](#) suggested that UDGs are part of the dwarf galaxy population, but with extreme spin properties. Strong outflows are proposed to be responsible for the termination of star formation and gas cooling at early cosmic time and for the formation of UDGs seen today ([Janowiecki et al. 2015](#); [Di Cintio et al. 2017](#)). Since UDGs have first been discovered in the Coma cluster, the processes confined to dense environment such as ram pressure and tidal stripping are likely important mechanisms for generating such galaxies. Recent progresses have reported the discovery of UDGs in various environments, not only in clusters. Of these works, [Smith Castelli et al. \(2016\)](#) reported two UDGs in a compact group (HCG 44), which is less dense than massive galaxy clusters. In addition, UDGs are found in even sparser environments, such as the vicinity of M101 ([Merritt et al. 2016](#)) and poor galaxy groups ([Román & Trujillo 2017b](#)). These works together demonstrate that UDGs do not exist exclusively in the cluster environments.

Hickson compact groups (HCGs) have a high density that is comparable to the center of clusters, and they have a low velocity dispersion similar to those of loose groups ($< \sigma > \sim 200 \text{ km s}^{-1}$), providing a unique environment to sustain galaxy evolution ([Hickson et al. 1992](#)). Members of HCGs may almost undergo continuous gravitational perturbations and show signs of enhanced activities such as like bluer optical colors or higher radio continuum power in the violently interacting galaxies and close pairs ([Verdes-Montenegro et al. 1997](#)). In addition, many HCGs contain a diffuse background light envelope in observations, and these diffuse envelopes may be stripped material from cluster member galaxies ([Da Rocha et al. 2005](#)). HCGs are also suggested to be favorable places for searching LSB galaxies and UDGs ([Ordenes-Briceño et al. 2016](#)).

We carry out a search for extreme LSB galaxies (including UDGs) in a field centered on HCG 95. Our observations cover a field of $3^\circ \times 3^\circ$. In this paper, we present 89 candidates of extreme LSB galaxies (with 57 plausible UDGs) found in deep g - and r -band imaging and their spatial distribution in the HCG 95 field. In Section 2 we describe the observation and data processing. UDG candidates are selected and their properties are given in Section 3, and in Section 4 we discuss our findings. Finally, we summarize our results in Section 5. We adopt an HCG 95 distance modulus of 36.05 mag (162.2 Mpc) with the following cosmology: $\Omega_M = 0.3$, $\Omega_\Lambda = 0.7$ and $H_0 = 70 \text{ km s}^{-1} \text{ Mpc}^{-1}$. We use the AB magnitude system throughout this work.

2. OBSERVATION AND DATA REDUCTION

Our imaging observations of a $3^\circ \times 3^\circ$ field centered on HCG 95 were taken with the Chinese Near Object Survey Telescope (CNEOST) of diameter 1.04/1.20 m in Xuyi Station (Zhang et al. 2013, 2014). The telescope is equipped with a $10\text{k} \times 10\text{k}$ STA 1600 CCD with 16 readout channels, providing a field of view (FOV) of $3^\circ \times 3^\circ$ and a pixel scale of $1''.029$. At the distance of HCG 95 (162.2 Mpc), this corresponds to a resolution of 0.784 kpc per pixel. The Sloan Digital Sky Survey (SDSS) g and r filters were chosen for the imaging observations over five nights from 2015 October 10 to 16. Each exposure takes 90 s. The integration time is 16.15 hr and 10.65 hr for g and r , respectively. Before the starting and after the end of every night, we obtained bias and dark images as well as sky flats throughout each filter.

The raw image data were reduced following standard procedures, including bias and dark subtraction, flat-fielding, and removal of bad/hot pixels. Each exposure image contains $10\text{k} \times 10\text{k}$ pixels divided into 16 regions to be read out. The effective gain of the readout channels differs slightly from each other. Sky flat frames are used to determine the effective gains of the readout channels. The raw images were corrected to have the same effective gain before flat-fielding. For the sky flat frames, we normalized each to the median of the central $6\text{k} \times 6\text{k}$ region and then divided by the best-fit slant plane to the same region in order to correct for the inhomogeneity within a single frame. Then these flat frames were combined together to generate the final flat. Again, the final flat was divided by the best-fit slant plane determined from the central $6\text{k} \times 6\text{k}$ region in order to remove systematic structures. The final flat frame is used for flat-fielding that removes pixel-to-pixel variations. Bad or hot pixels were identified with values below 0.9 or above 1.1 in the final flat frame. Perfect flat-fielding could improve the detection depth for faint structure because the detection limit is constrained by systematic errors, which are dominated by flat-fielding (Abraham & van Dokkum 2014). The vignetting effect becomes significant at the edges of a wide-field image. This effect can be mostly corrected for through flat-fielding.

A catalog of 12,922 stars in the HCG 95 field from SDSS is used as the reference to determine astrometric distortions and calibration. Source detection and photometry was done using the software SExtractor (Bertin & Arnouts 1996), and SCAMP (Bertin et al. 2006) was used to compute an astrometric solution for individual science images, giving a typical accuracy of $\text{RMS} = 0''.1$ in astrometry. Only bright stars of $14 < g < 18$ mag with photometry from SDSS are adopted

as the reference sources for photometric calibration. All science images were calibrated to have a constant photometric zero point $zp = 25.0$ mag. We fit a slant plane to the background and subtracted it from each image. This helps to reduce systematic errors in image combination. Weight images were generated to mask bad/hot pixels and saturated pixels. Cross-talks caused by saturated stars were removed following Freyhammer et al. (2001).

Finally, we selected the good-quality science images and stacked those of the same filter together using the software tool SWARP (Bertin et al. 2002), yielding the final g - and r -band science images with effective integration times of 13.15 hr and 9.525 hr, respectively. The 3σ depth of the two images (in a $10'' \times 10''$ box) reaches $\mu(g) \sim 29.16$ mag arcsec $^{-2}$ and $\mu(r) \sim 28.38$ mag arcsec $^{-2}$, respectively. The depths are comparable to those given in Fliri & Trujillo (2016) and Koda et al. (2015). The $g + r$ combined image is shown in the left panel of Figure 1.

The FWHM of the point spread function (PSF) is typically $4''$ and $3''$ in the central region of the g - and r -band science image, respectively. We note that the PSF of the images obtained with CNEOST slightly increases from the center to the edges of the FOV. We use stars identified from SDSS to trace the PSF variation and build the 2-dimensional map of PSF FWHM through best fitting a third-order polynomial function to the FWHM map of the selected stars. The best-fit PSF FWHM maps in g and r are shown in the Appendix in Figure A.1.

3. UDG CANDIDATES

Our goal is to search for UDGs that have large sizes and very LSB. We run SExtractor (Bertin & Arnouts 1996) in dual mode with the configuration optimized for the detection of extended LSB objects and extract source catalogs from the stacked science images. The g -band image is used for source detection because it is somewhat deeper and has a slightly better resolution (see Figure A.1). We limit the source detection to the central area of diameter $< 2''.5$ to minimize the edge effects (such as vignetting or comatic aberration). We obtained the g - and r -band photometric catalogs consisting of 31,230 objects.

The widely used criteria for UDGs selection are $r_e > 1.5$ kpc and $\mu(g, 0) > 24.0$ mag arcsec $^{-2}$ (van Dokkum et al. 2015a). Given that UDGs generally obey a rather flat profile, we average the total magnitude over the area within the PSF-corrected half-light radius as the central surface brightness, following van Dokkum et al. (2015a). We cross correlate our catalog with the photometric catalog of the same field from the SDSS with a tolerance

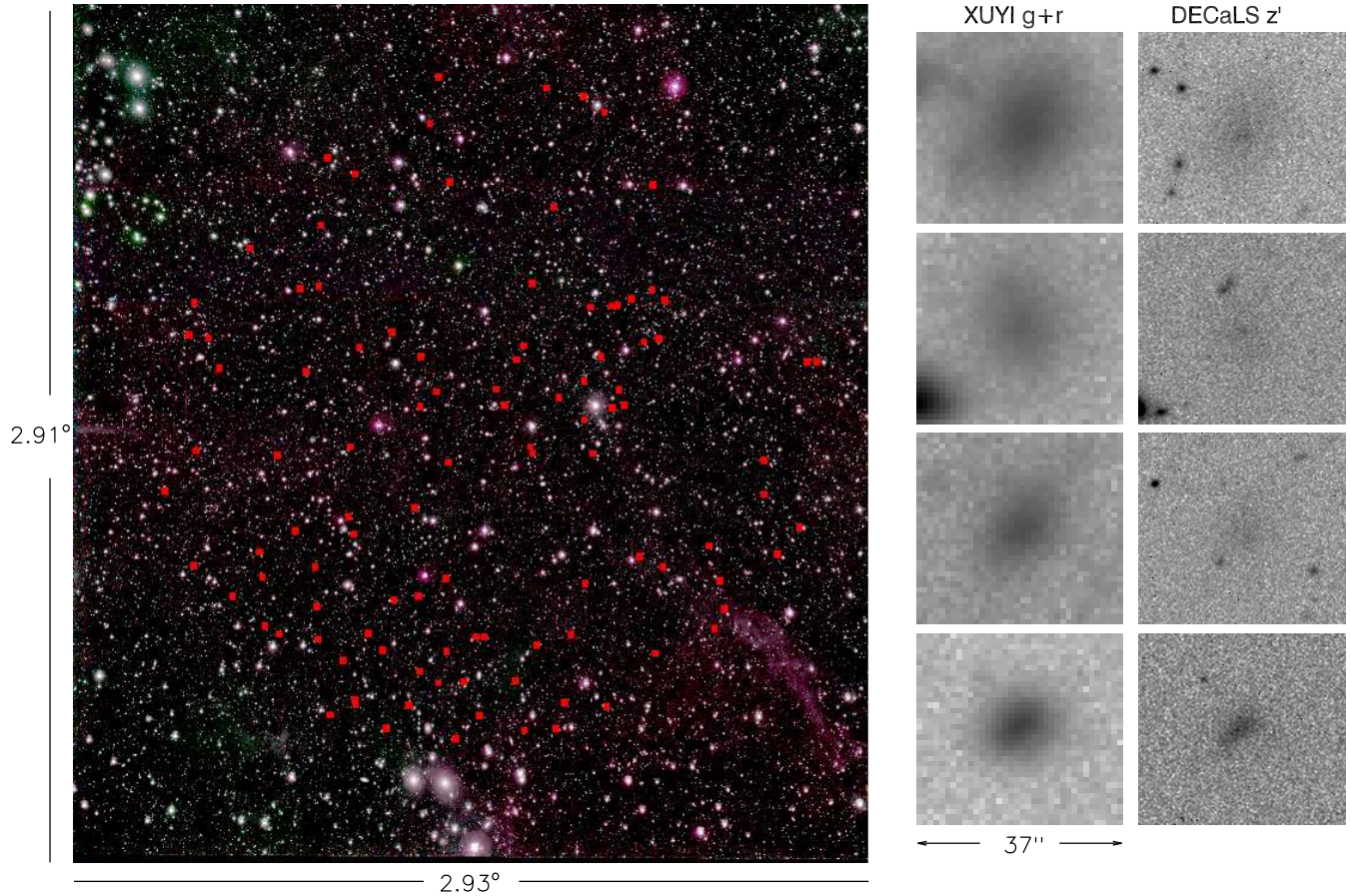


Figure 1. Left: the deep $g+r$ color image of the HCG 95 field covering a sky area of $2^\circ 93 \times 2^\circ 91$. Red squares mark the 105 UDG candidates. Right: typical UDGs viewed in the images from Xuyi and the Dark Energy Camera Legacy Survey (DECaLS). The size of the postage stamp images is $37'' \times 37''$.

radius of $r = 1''.5$, and exclude stars, bright sources with $\mu(g, 0) < 24.0 \text{ mag arcsec}^{-2}$, and compact sources with $r_e < 1''.92$. Here the cut $1''.92$ corresponds to a size of 1.5 kpc at the distance of HCG 95. The objects in our catalog with stellarity parameter $\text{CLASS_STAR} > 0.15$ are classified as compact/point sources and those with a color out of $g-r < 0$ or $g-r > 1.2$ are treated as false sources, including noise contaminators and sparks from bright sources. We obtained 464 SDSS-detected galaxies of $\mu(g, 0) > 24.0 \text{ mag arcsec}^{-2}$ and $r_e > 1''.92$, and 1771 μ sources from our deep g and r observations without detection in the SDSS. For the preselected 2235 sources, we estimated the intrinsic half-light radii and central surface brightness from our deep g -band image to further identify UDGs. The size measurement for galaxies needs to correct the broadening effect by PSF. We extracted the PSF size from the 2D PSF FWHM maps shown in Figure A.1 for the objects of given positions. We roughly estimated the intrinsic ef-

fective radius with $r_e = \sqrt{r_{\text{obs}}^2 - R_{\text{psf}}^2} > 1''.92$ following Bouché et al. (2015), where r_{obs} is the directly observed half-light radius, and R_{psf} is the half-light radius of the PSF (see Figure A.3 for more details). We estimated that 644 of the 2235 objects satisfy $r_e > 1''.92$ and $\mu(g, 0) > 24.0 \text{ mag arcsec}^{-2}$.

We realize that the preselected 644 objects that satisfy the selection criteria for UDGs may still be contaminated by blended sources. In particular, the low resolution of our deep g - and r -band images together with the source detection configured for extended sources would often mistake blended faint sources as UDG candidates. On the other hand, the degradation of the image quality toward the edges of the images increases the uncertainties in identification of UDGs. We visually inspect the preselected targets with the aid of SDSS DR12 Image

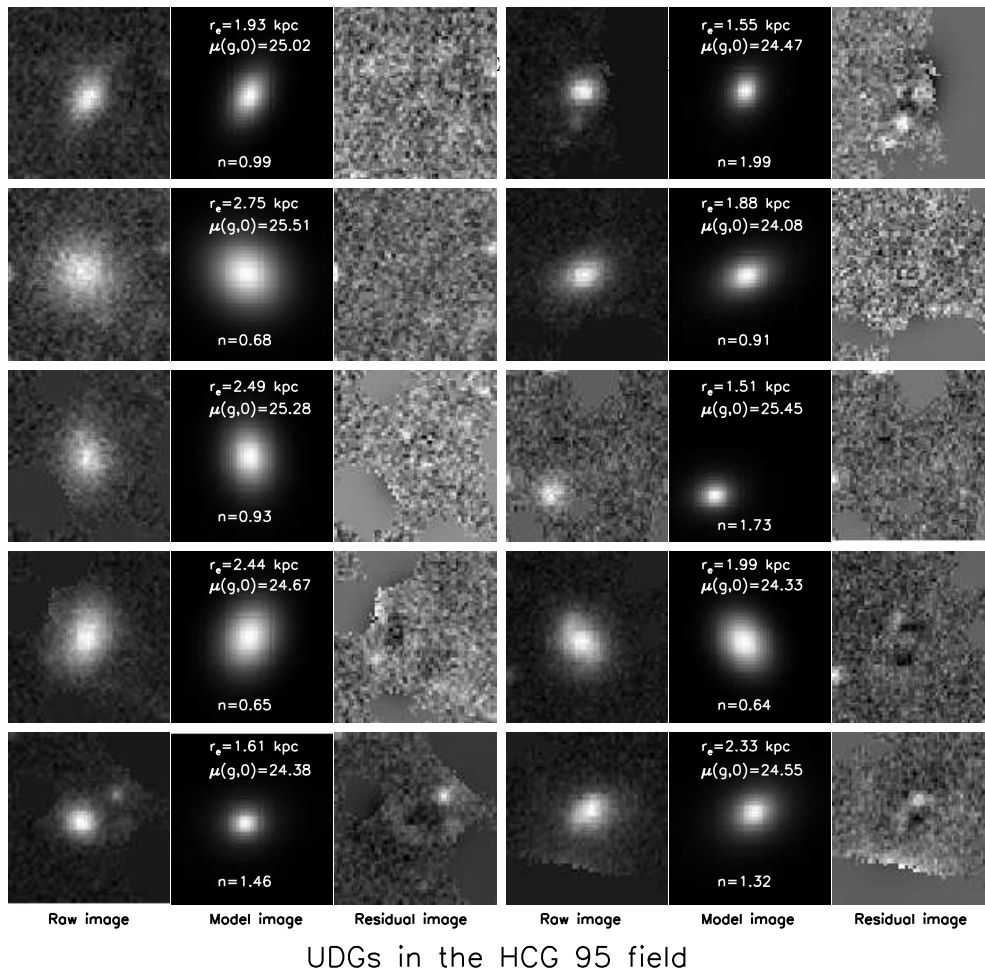


Figure 2. Ten examples of GALFIT models to UDG images. The three columns from left to right show the g -band image, the GALFIT model, and the residual image. The best-fit Sérsic profiles are described by the half-light radius r_e (kpc), the central surface brightness $\mu(g,0)$ (in units of mag arcsec^{-2}), and the Sérsic index n . The size of every postage stamp image is $56'' \times 56''$.

List Tool¹ to examine their morphologies. Removing binary sources and other artifacts of misclassification, we obtained a sample of 105 UDG candidates over an area of 4.9 degree^2 in the HCG 95 field.

Considering the uncertainties due to the variation of PSF FWHM in our observations, we examine our results by measuring the central surface brightness of UDGs using GALFIT (Peng et al. 2002). The averaged PSF in the central region of our deep g -band science image is used. The central surface brightness is then extracted from the model Sérsic profile (Graham & Driver 2005; Zhong et al. 2008). Finally, we obtain the g -band central surface brightness for 89 of the 105 UDGs, as shown in Figure 2.

The HCG 95 field is covered by the Dark Energy Camera Legacy Survey (DECaLS) (Blum et al. 2016), which provides seeing-limited z' -band images obtained with the 4 m Blanco telescope. Of the 89 UDG candidates, 84

have z' -band images from Data Release 3 (DR3)². We measured the half-light radius from their z' -band images and list the results in Table A.1, confirming that they have very LSB. Four examples of UDG candidates are shown in the right panel of Figure 1.

Finally, we identify 89 UDG candidates in the HCG 95 field. Redshift information is required to determine whether they are associated with HCG 95. As shown in Figure 3, HCG 95 is a compact group ($\alpha(\text{J2000}) = 23^{\text{h}}19^{\text{m}}31.73^{\text{s}}$ and $\delta(\text{J2000}) = +9^{\circ}29'30''.7$, redshift $z = 0.0396$) with four bright galaxies seen in the central region. Of the four galaxies, H95A is a giant elliptical galaxy. H95C appears to contain double nuclei, therefore it is considered to be a merger remnant of two disk galaxies (Iglesias-Páramo & Vilchez 1997, 1998). H95C has two obvious tidal tails and a bridge connecting it to H95A (Rodrigue et al. 1995). H95B is a foreground galaxy because its line-of-

¹ <http://skyserver.sdss.org/dr12/en/tools/chart/listinfo.aspx>

² <http://legacysurvey.org/dr3/description/>

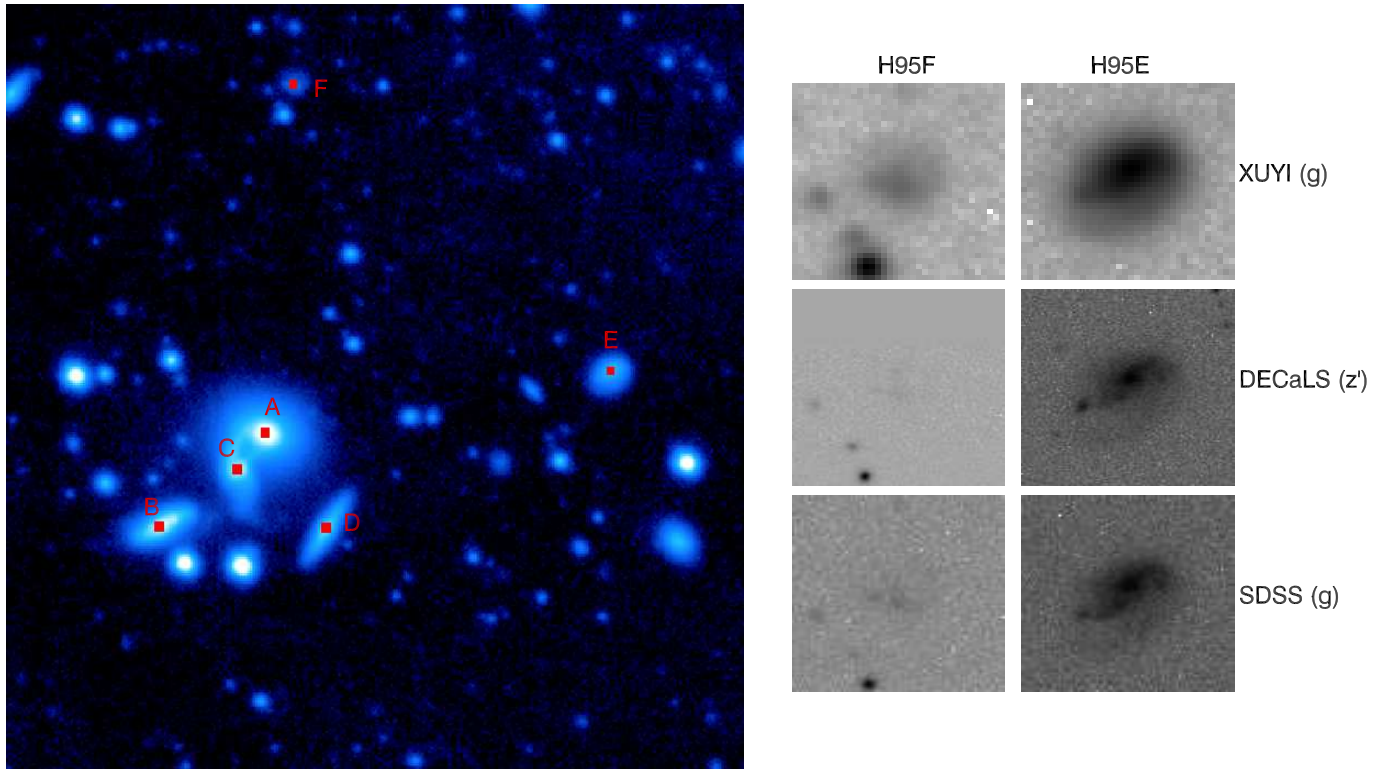


Figure 3. Distribution of member galaxies for HCG 95. Left: members of HCG 95; the region is $6'.7 \times 6'.7$, and the top of red point is H95F, the UDG with HI distribution. Right: H95F and H95E are detected by the Xuyi telescope, DECaLS, and SDSS; the size of the postage stamp images is $37''$.

sight velocity significantly differs from the velocity of the other members (Iglesias-Páramo & Vílchez 1997; Da Rocha et al. 2005). H95D is an edge-on spiral galaxy (Iglesias-Páramo & Vílchez 1997). Many observations have been made of HCG 95, including HI, H α and X-ray (Ponman et al. 1996; Iglesias-Páramo & Vílchez 1998, 2001; Huchtmeier et al. 2000; Da Rocha et al. 2005). Interestingly, three structures can be found in the HCG 95 field, including the Pegasus I cluster (Chincarini et al. 1976; O’Neil et al. 1997), the Pegasus II cluster (Richter & Huchtmeier 1982), the Abell 2588 cluster (Richter & Huchtmeier 1982; Abell et al. 1989). These overdensities provide various environments in which to search for UDGs.

In the $3^\circ \times 3^\circ$ field centered at HCG 95, there are 96 nearby galaxies with known redshift from the literature, including 29 NGC galaxies and those from the Update Zwicky Catalogue (UZC) catalog (Falco et al. 1999), from the Flat Galaxy Catalog (FGC), the Uppsala Galaxy Catalog (UGC), from the SDSS, and from the Arecibo Legacy Fast ALFA (ALFALFA) (Haynes et al. 2011; Teimoorinia et al. 2017). The 29 NGC galaxies

are listed in Table 1. The spatial distributions of these nearby galaxies are shown in Figure 4. We can see that these galaxies are located in two distinct redshift bins $0.009 < z < 0.016$ and $0.034 < z < 0.045$, which are associated with Pegasus I ($z \sim 0.013$) and Pegasus II ($z \sim 0.040$, similar to HCG 95) (Richter & Huchtmeier 1982; Canizares et al. 1986), as shown in Figure 5. Moreover, the two groups of galaxies are also globally separated from each other; this split is shown by the dotted line in Figure 4. We thus conclude that HCG 95 is a part of the poor galaxy cluster Pegasus II and our UDG candidates are most likely associated with either Pegasus I at $z \sim 0.013$ or Pegasus II at $z \sim 0.040$. Indeed, from Figure 4 one can see that the UDG candidates (red open circles) are also clustered with the two structures, supporting that the UDG candidates reside in the two poor galaxy clusters.

We note that our selection criteria for UDGs are based on the distance of HCG 95 (i.e., the Pegasus II cluster). However, Pegasus I locates is located at a distance closer than Pegasus II. Accordingly, the physical sizes of UDG candidates associated with Pegasus I would be

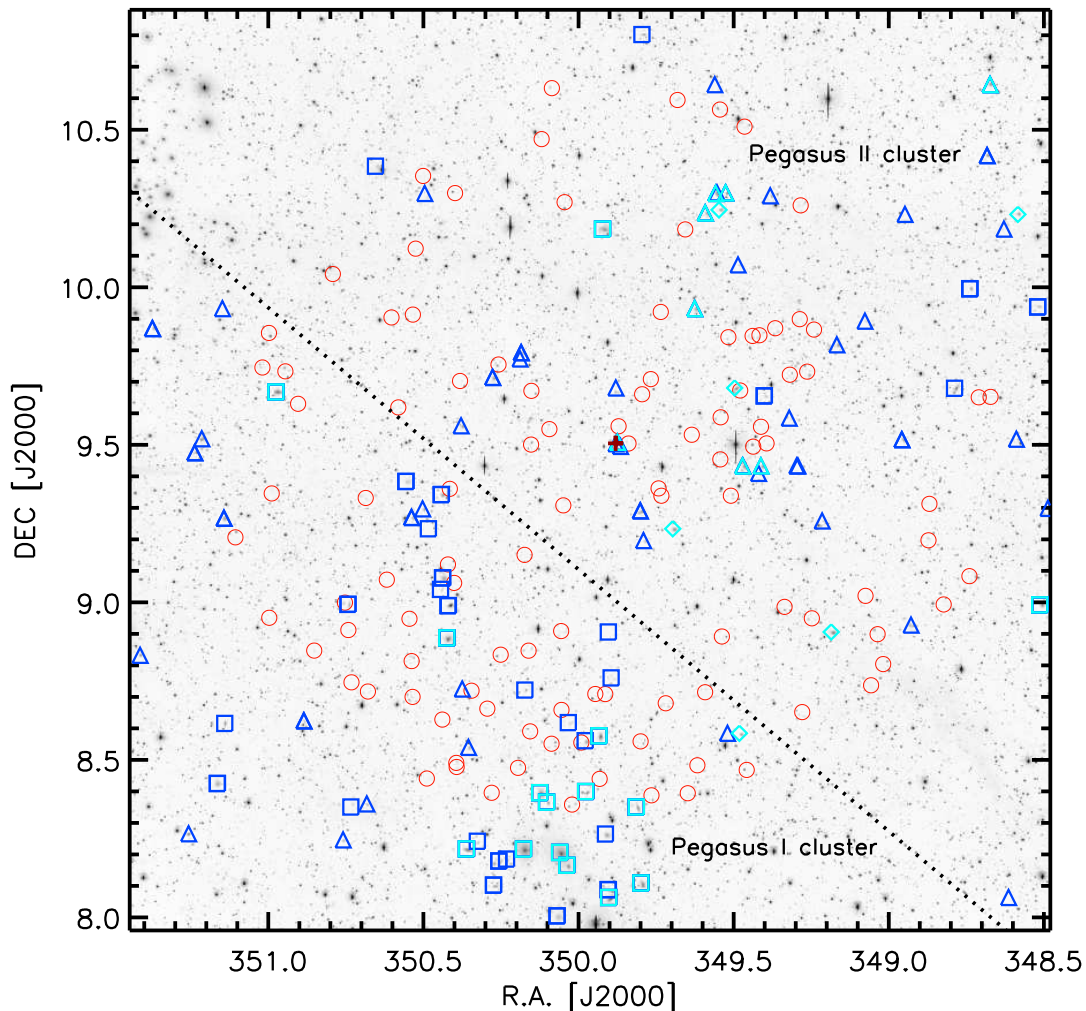


Figure 4. Spatial distribution of our 89 candidates of UDGs (red circles). The group HCG 95 is marked by the plus at the center. Squares represent nearby galaxies with $0.009 < z < 0.016$. Triangles show nearby galaxies with $0.034 < z < 0.045$. These nearby galaxies are associated with the poor galaxy clusters Pegasus I (squares) at $z = 0.013$ and Pegasus II (triangles) at $z = 0.040$. Of these, 29 are included in the NGC catalog and are shown with cyan symbols. The dotted line is a crude guide to separate the two galaxy clusters.

smaller. There are 44/45 UDG candidates located below/above the dotted line in Figure 4, likely associated with Pegasus I/Pegasus II. When the distance of Pegasus I ($z = 0.013$, $D = 55.2$ Mpc, $m - M = 33.51$ mag) is adopted to calculate the size and luminosity, 12 of the 44 UDG candidates still satisfy the UDG selection criterion $r_e > 1.5$ kpc. The remaining 32 would be very LSB galaxies with sizes smaller than the size of a typical UDG. The 45 candidates above the dotted line would be UDGs if they are located close to Pegasus II. The sum of two parts would mean that 57 UDGs are located in the HCG 95 field. We caution that member galaxies of the two clusters are widely spread over the field and information on the redshift is necessary to decide the real membership and physical size for a given UDG candidate.

Still, the estimate of UDG numbers should be reasonable in a statistic manner. For simplification, we assume that all 44 UDG candidates in the Pegasus I region are at a distance of $z = 0.013$ and all 45 UDG candidates in the Pegasus II region at a distance of $z = 0.040$. Table A.1 lists the measured properties of our sample of 89 targets and denotes them to be either UDGs or very LSB galaxies. In short, we conclude that roughly $\sim 50 - 60$ galaxies are identified to be UDGs associated with the two poor galaxy clusters in the HCG 95 field.

Table 1. Properties of the 29 NGC galaxies in the HCG 95 field collected from the NASA Extragalactic Database (NED).

Name (NGC/IC)	R.A. (J2000.0)	Decl. (J2000.0)	z	$m - M$ (mag)
7612	23:19:44.2	+08:34:35	0.0107	32.97
7611	23:19:36.7	+08:03:48	0.0108	33.00
7634	23:21:41.9	+08:53:14	0.0108	32.98
7626	23:20:42.6	+08:13:01	0.0114	33.11
7608	23:19:15.3	+08:21:02	0.0117	33.18
7610 ^a	23:19:41.5	+10:11:05	0.0119	33.22
7648 ^b	23:23:54.1	+09:40:04	0.0119	33.22
7631	23:21:26.8	+08:13:03	0.0125	33.35
7623	23:20:30.1	+08:23:46	0.0125	33.34
7619	23:20:14.6	+08:12:23	0.0125	33.35
7621	23:20:24.7	+08:21:57	0.0128	33.40
7617	23:20:09.1	+08:09:56	0.0139	33.60
5309	23:19:11.8	+08:06:33	0.0140	33.62
7615	23:19:54.5	+08:23:58	0.0149	33.77
7529	23:14:03.2	+08:59:32	0.0151	33.81
7569	23:16:44.5	+08:54:22	0.0217	34.66
5306	23:18:11.3	+10:14:44	0.0253	35.02
7586	23:17:55.6	+08:35:04	0.0267	35.14
7601	23:18:47.1	+09:14:01	0.0268	35.15
7528	23:14:20.1	+10:13:53	0.0292	35.35
7587	23:17:59.3	+09:40:49	0.0292	35.35
5305	23:18:06.3	+10:17:59	0.0350	35.77
7594 ^c	23:18:14.0	+10:17:52	0.0362	35.84
7542	23:14:41.7	+10:38:35	0.0395	36.05
7609	23:19:29.9	+09:30:29	0.0396	36.05
7595	23:18:30.2	+09:55:56	0.0410	36.13
7579	23:17:38.9	+09:25:59	0.0411	36.14
5307	23:18:22.0	+10:14:09	0.0413	36.17
7584	23:17:53.1	+09:25:58	0.0431	36.25

^a NGC 7610 and NGC 7616 refer to the same object;

^b NGC 7648 = IC 1486;

^c NGC 7594 = IC 1478.

We examine the properties of our sample of UDGs and very LSB galaxies in comparison with other samples of UDGs in the literature. Figure 6 shows the absolute magnitude M_g in relation to the average surface brightness μ_e and effective radius r_e . Figure 7 presents

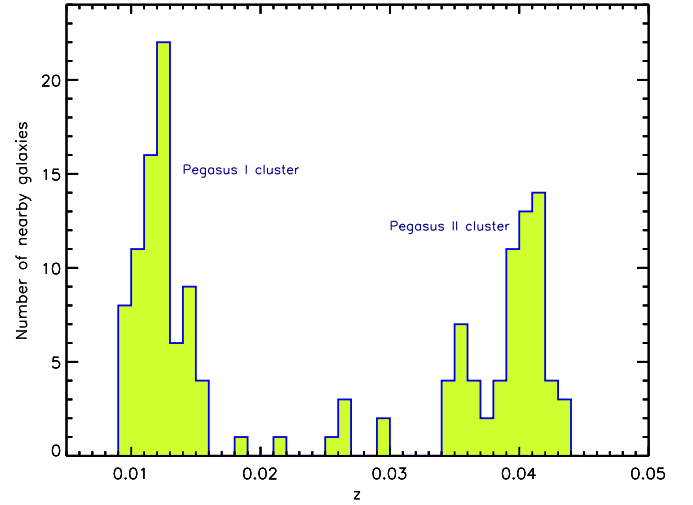


Figure 5. Histogram of nearby galaxies in the HCG 95 field. These galaxies are divided into two distinct structures, we term them the Pegasus I/Pegasus II (Pegasus I at $z=0.013$ and Pegasus II at $z=0.040$) clusters.

the central surface brightness $\mu(g, 0)$ in relation to the effective radius r_e . From Table A.1 we can see that the 32 very LSB galaxies in our sample are characterized by $\mu(g, 0) = 24.00 - 26.45 \text{ mag arcsec}^{-2}$, typical $\langle r_e \rangle \sim 0.98 \text{ kpc}$, typical $\langle M_g \rangle \sim -13.24 \text{ mag}$, color $\langle g - r \rangle \sim 0.65$, and axis ratio $\langle b/a \rangle \sim 0.75$; while the 12 UDGs have $\mu(g, 0) = 24.08 - 26.19 \text{ mag arcsec}^{-2}$, $\langle r_e \rangle \sim 1.93 \text{ kpc}$, $\langle M_g \rangle \sim -14.66 \text{ mag}$, $\langle g - r \rangle \sim 0.69$ and $\langle b/a \rangle \sim 0.71$; and the 45 UDGs in Pegasus II have $\mu(g, 0) = 24.00 - 25.88 \text{ mag arcsec}^{-2}$, $\langle r_e \rangle \sim 2.98 \text{ kpc}$, $\langle M_g \rangle \sim -15.90 \text{ mag}$, $\langle g - r \rangle \sim 0.56$ and $\langle b/a \rangle \sim 0.67$. The comparisons in Figures 6 and 7 confirm that the selected UDGs in the HCG 95 field are distinct from normal galaxies in terms of these parameters and comparable to those found in previous studies (e.g., van der Burg et al. 2016). The consistence indicates that UDGs can be found in different environments.

Figure 8 presents the r -band absolute magnitude versus $g - r$ for our UDGs in comparison with other galaxy populations, including nearby galaxies from the SDSS and HI gas-rich galaxies from the ALFALFA survey. Our sample UDGs are spread over a wide range in $g - r$, similar to the spread of member galaxies of the poor galaxy clusters Pegasus I and Pegasus II. A sample of nearby mass-selected galaxies with $0.001 < z < 0.06$ are also presented for comparison. It is clear from Figure 8 that our sample contains >20 UDGs with colors similar to the colors of star-forming galaxies, although most UDGs are as red as quiescent dwarf galaxies. The UDGs

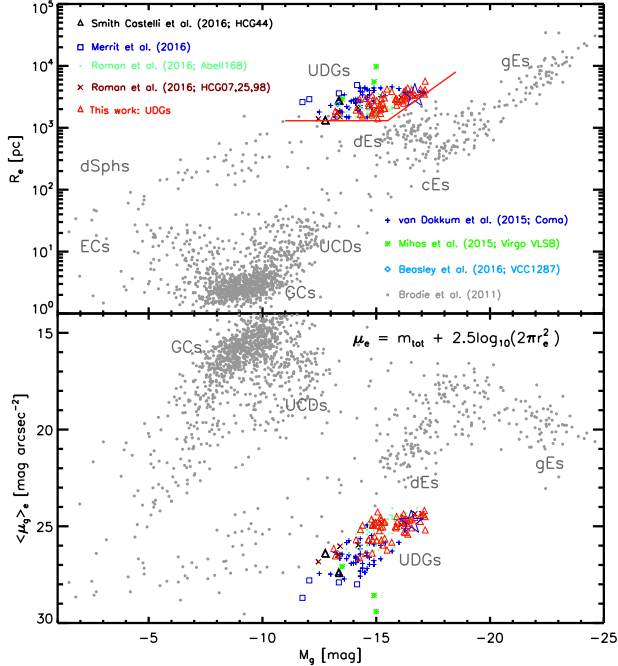


Figure 6. Comparison of UDGs with other galaxy populations in diagrams of absolute magnitude in g vs. effective radius and average surface brightness. The gray dots are quiescent galaxies from Brodie et al. (2011); blue pluses represent 47 UDGs from the Coma cluster (van Dokkum et al. 2015a); green tail symbols are the extremely LSB galaxies from Mihos et al. (2015); the light blue diamond refers to the single UDG from Beasley et al. (2016); black triangles show 2 UDGs found in the HCG 44 field (Smith Castelli et al. 2016); blue squares represent the 4 UDGs in the M101 field (Merritt et al. 2016); light green dots are 80 UDGs from Abell 168 (Román & Trujillo 2017a); brown crosses are 11 UDGs from HCG 07, 25, and 98 (Román & Trujillo 2017b); and red triangles denote UDGs from this work.

in the Pegasus II cluster appear to be slightly bluer in $g - r$ than the UDGs in the Pegasus I cluster. The diversity of color indicates that UDGs may be formed through different star formation histories, which are to some extent coupled with the environments.

Figure 9 shows the $r - z'$ versus $g - r$ diagram for 89 UDG candidates and 96 spectroscopically identified nearby galaxies in the HCG 95 field. We can see that the 89 UDG candidates tend to be fainter and bluer than the nearby galaxies (as shown in Figure 8), although the dispersion in two colors is rather large. We also show the color tracks of galaxy models of different ages from BC03 (Bruzual & Charlot 2003). The single stellar population (SSP) and an e-folding ($\tau=1$ Gyr) evolutionary history are adopted to generate the templates. The metallicity is set to be solar and 1/5 solar for comparison. The

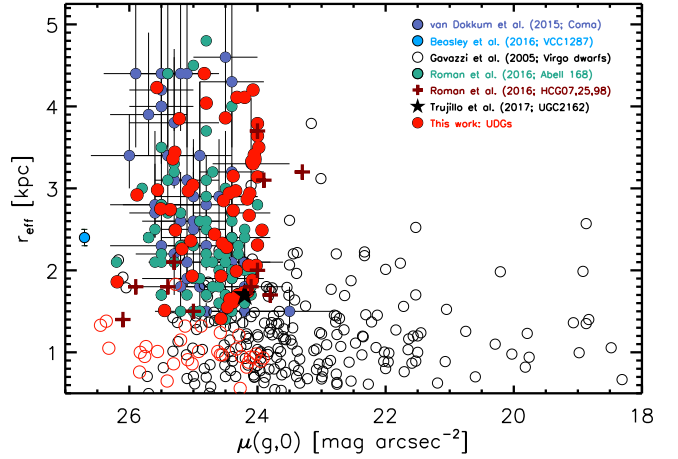


Figure 7. Relationship between half-light radius and g -band central surface brightness. The black open circles represent Virgo dwarfs (Gavazzi et al. 2005); the blue solid circles are UDGs from Coma cluster (van Dokkum et al. 2015a); indigo solid circles are UDGs from the Abell 168 cluster (Román & Trujillo 2017a); the light blue solid circle refers to the UDG in the Virgo cluster from Beasley et al. (2016); and brown pluses represent 11 UDGs from HCG 07, HCG 25, and HCG 98 (Román & Trujillo 2017b). Red solid circles mark our UDGs and red open circles represent the very LSB galaxies (possible UDGs) in this work.

typical ages of 0.1, 0.3, 1, 3, 6, 12 Gyr are marked with solid circles. We note that the z' -band photometry has large uncertainties for the faint UDG candidates and the dispersion in color $r - z'$ is largely driven by the measurement errors. We note that the model templates are only for stellar emission. The presence of strong emission lines in the r band (i.e. $H\alpha + [NII]$) would apparently make galaxies appear bluer in $r - z'$ and redder in $g - r$. It is obvious that a large fraction of UDG candidates have young stellar populations ($< \sim 3$ Gyr), and nearly one-third are as blue as blue-cloud galaxies.

We derived the stellar mass M_* from luminosity and color using the mass-to-light ratio versus $g - r$ relation (Bell et al. 2003; Taylor et al. 2011). The typical stellar mass is $M_* \sim 4.32 \times 10^7 M_\odot, 1.58 \times 10^8 M_\odot,$ and $3.72 \times 10^8 M_\odot$ for 32 very LSB galaxies, 12 UDGs in Pegasus I, and 45 UDGs in Pegasus II, respectively. The stellar masses of UDGs are consistent with previous studies (van Dokkum et al. 2015a; Román & Trujillo 2017a,b). Combined together, our results suggest that UDGs not only exist in galaxy clusters such as Coma, Virgo, Fornax, and Abell (Mihos et al. 2015; Muñoz et al. 2015; Koda et al. 2015; van Dokkum et al. 2015a,b; Martínez-Delgado et al. 2016; Janssens et al. 2017), but also live in lower density environments.

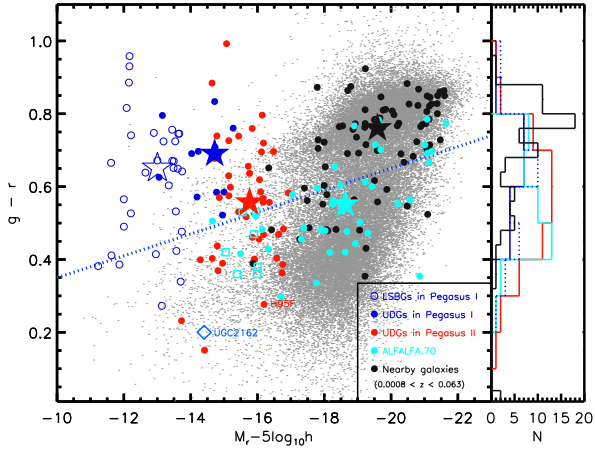


Figure 8. Diagram of color $g-r$ vs. absolute magnitude in r for our UDGs and nearby galaxies. The gray points represent the galaxies with $0.001 < z < 0.06$ from the SDSS. The blue dotted line is adopted from Blanton et al. (2006) to split the SDSS galaxies into red sequence and blue cloud. Our sample of 89 UDG candidates are divided into subsamples, including 32 extremely LSB galaxies in the Pegasus I region (blue open circles), 12 UDGs at the distance of Pegasus I (blue solid circle), and 45 UDGs at the distance of Pegasus II (red solid circles). Galaxies with rich HI gas from the ALFALFA survey are shown with cyan solid circles. The cyan squares are the UDGs with strong HI emission from the ALFALFA catalog (Leisman et al. 2017). The confirmed member galaxies of two poor galaxy clusters in the HCG 95 field are also shown (black solid circles). The median of $g-r$ for each subsample of UDGs is marked with large star symbols. The light blue square is a blue UDG from Trujillo et al. (2017). The right panel presents the number distribution of color from these subsample.

Observations of neutral hydrogen gas are available for the galaxy group HCG 95 (Huchtmeier et al. 2000). Two member dwarf galaxies H95E and H95F about $3\frac{1}{5}$ offset from the center of HCG 95 (about 164.6 kpc at the distance of HCG 95), as shown in Figure 3, have been detected to have strong HI emission with the Very Large Array (VLA). The line-of-sight velocities of the two galaxies are $11830 \pm 5 \text{ km s}^{-1}$ and $11730 \pm 5 \text{ km s}^{-1}$, respectively. From the VLA observations, we derive the HI gas mass for H95E and H95F using the formula $(M_{\text{HI}}/M_{\odot}) = 2.36 \times 10^5 (f/\text{Jy km s}^{-1})(D/\text{Mpc})^2$ (Levy et al. 2007), where f is the 21 cm line flux (in Jy km s^{-1}) and D is the distance of HCG 95. The derived HI mass is 2.02 and $1.08 \times 10^9 M_{\odot}$ for H95E and H95F, respectively.

Interestingly, H95F is one of our sample UDGs. The properties of H95F are given in Table 2. In addition, H95F is a blue dwarf galaxy with $g-r \sim 0.28$ and $M_{\star} \sim 1.82 \times 10^8 M_{\odot}$. We further address the

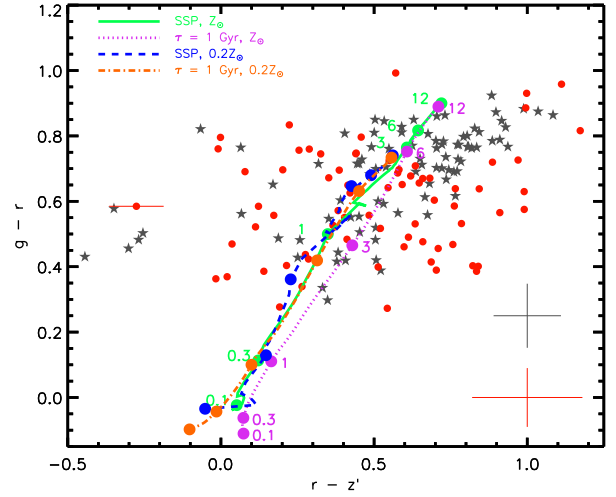


Figure 9. Color-color diagram of UDGs and spectroscopically identified nearby galaxies in the HCG 95 field. The gray stars represent the nearby galaxies with redshifts $0.009 < z < 0.05$. The red solid circles show the 89 UDG candidates. BC03 model color tracks are shown for the single stellar population. The green solid line and the magenta dotted line denote the evolution tracks for SSP at one solar metallicity. The blue dotted line and the orange dash-dotted line show the evolution tracks for SSP at metallicity $0.2Z_{\odot}$. The magenta dotted line and orange dash-dotted line give different metallicity τ models with $\tau = 1 \text{ Gyr}$. The gray and red error bars at the bottom right denote the 0.5σ dispersion of the galaxies.

connections between UDGs and gas-rich LSB galaxies. Impey et al. (1996) have compiled a sample of 693 LSB galaxies at $z \lesssim 0.1$. We find that 16 extended LSB galaxies in this sample meet the selection criteria of UDGs, and 15 of them have an HI detection. The physical parameters of the 16 UDGs along with H95F are given in Table 2. They have HI gas masses from $5.13 \times 10^7 M_{\odot}$ to $3.39 \times 10^9 M_{\odot}$ and stellar masses over the range of $10^6 - 10^8 M_{\odot}$ derived from color and luminosity (Fukugita et al. 1996; Bell et al. 2003; Taylor et al. 2011). Recently, Trujillo et al. (2017) have reported one nearest UDG (UGC 2162) with strong HI emission; the properties of this UDG are also listed in Table 2. Leisman et al. (2017) presented 115 UDGs with HI emission from the ALFALFA survey. We include 7 of the 115 UDGs in Table 2 for a comparison. The overlap of UDGs with some extremely LSB galaxies detected by HI surveys in size and central surface brightness reveals an intimate connection between the two populations, providing key insights into the formation of UDGs in the local universe (Bellazzini et al. 2017).

Motivated by the finding that H95F is an HI gas-rich galaxy, we cross-correlated our sample of 89 UDG

Table 2. Comparison of H95F with the extremely LSB galaxies (Can Be Seen as UDGs) with HI gas detection from [Impey et al. \(1996\)](#).

Name	R.A. (J2000.0)	Decl. (J2000.0)	$\mu(B, 0)$ (mag arcsec ⁻²)	m_B (mag)	M_B (mag)	Velocity (km s ⁻¹)	r_e ($''$)	r_e (kpc)	$\log(M_{\text{HI}})$ (M_{\odot})
H95F ^a	23:19:29.0	+9:33:31	24.1	19.4	-16.7	11730	4.35	3.41	9.03
UGC 2162 ^b	2:40:23.1	+01:13:45	24.4	16.1	-15.0	1172	28	1.7	8.28
322019 ^c	22:58:26.9	+01:50:58.9	24.6	18.5	-15.8	4819	11.9	3.9	8.81
103796 ^c	00:20:39.6	+06:57:56.8	24.2	18.3	-16.2	5647	9.2	3.5	8.86
113790 ^c	01:13:02.1	+27:38:12.8	24.3	18.8	-15.4	4952	7.1	2.4	8.57
114905 ^c	01:25:18.5	+07:21:37	24.9	18.2	-16.2	5435	12.8	4.7	9.11
114943 ^c	01:47:06.6	+07:19:51.9	24.5	18.9	-16.4	8416	8.0	4.5	9.10
113949 ^c	01:49:38.6	+30:40:50.8	24.3	19.2	-15.8	7380	5.0	2.5	9.03
122966 ^c	02:09:29.0	+31:51:10	25.4	18.4	-16.4	6518	11.6	5.1	9.00
0139+0240	1:39:58.9	+2:40:40	24.4	16.9	-14.3	1765	26.0	3.15	8.60
0221+0034	2:21:49.8	+0:34:41	24.7	17.3	-17.5	8996	18.9	11.35	9.25
0225-0049	2:25:45.6	-0:49:50	25.0	18.0	-12.8	1464	13.2	1.33	7.71
0227+0040	2:27:01.1	+0:40:56	24.8	18.1	-16.6	8503	13.7	7.79	9.53
0249+0146	2:49:45.0	+1:46:16	24.5	16.5	-16.7	4293	21.2	6.19	8.87
0319+0015	3:19:14.2	+0:15:00	24.4	18.4	-15.7	6548	8.3	3.66	9.24
0955+0155	9:55:54.5	+1:55:58	24.9	17.2	-14.1	1815	18.3	2.28	8.54
1101+0211	11:01:45.4	+2:11:24	24.1	18.2	-16.2	7578	10.9	5.54	9.17
1110-0017	11:10:14.1	-0:17:47	24.8	17.8	-16.9	8472	11.6	6.57	9.37
1154+0203	11:54:48.6	+2 03:35	24.5	17.7	-13.8	1980	12.1	1.64	8.15
1228+0116	12:28:43.1	+1:16:13	25.1	18.3	-13.5	2289	11.1	1.74	8.20
1230-0015	12:30:34.2	-0:15:28	24.1	16.5	-16.1	3279	25.0	5.60	8.66
1249+0233	12:49:49.9	+2:33:34	25.0	19.1	-15.1	6971	10.4	4.84	8.91
1350+0230	13:50:59.7	+2:30:20	24.8	18.5	-14.8	4507	11.4	3.49	8.62
1431+0142	14:31:20.5	+1:42:25	25.8	17.4	-14.0	1829	24.2	3.04	8.30
1307+0112	13:07:31.2	+1:12:53	24.2	18.2	-15.6	5842	9.7	3.83	...

^a H95F is shown in this work.^b Measured in the g band, UGC 2162 from [Trujillo et al. \(2017\)](#).^c Measured in the g band from [Leisman et al. \(2017\)](#).

candidates with the HI galaxy catalog from the ALFALFA survey ([Giovanelli et al. 2005](#); [Haynes et al. 2011](#); [Teimoorinia et al. 2017](#)). Although 49 nearby galaxies with $0.009 < z < 0.058$ in the HCG 95 field are found to have an HI detection by ALFALFA, none of our sample UDGs is detected in ALFALFA. Deeper HI surveys will probably detect more UDGs with HI gas.

We compare the abundances of UDGs of three galaxy structures in the HCG 95 field with those of other groups and clusters from the literature. Figure 10 shows the

abundance of UDGs as a function of halo mass adopted from [Janssens et al. \(2017\)](#) and [van der Burg et al. \(2016\)](#), following a relation of $N \propto M_{200}^{0.93 \pm 0.16}$. It is clear that more massive halos host more numerous UDGs. We use the velocity dispersion to estimate the halo masses of the three structures in the HCG 95 field. The halo masses of galaxy group HCG 95 and the two poor galaxy clusters Pegasus I and II are $2 \times 10^{13} M_{\odot}$, $3 \times 10^{14} M_{\odot}$, and $5 \times 10^{14} M_{\odot}$, respectively ([Chincarini et al. 1976](#); [Girardi et al. 1998](#); [Barnes et al. 1999](#); [Randall et al.](#)

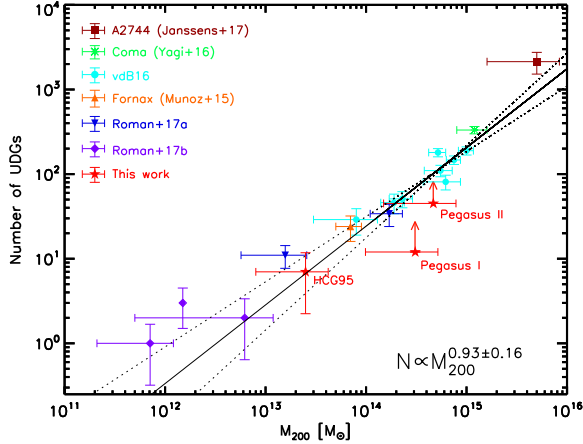


Figure 10. Abundance of UDGs as a function of halo mass. The red solid stars show the abundance of UDGs from this work, while the other symbols are obtained from the other clusters and groups. The solid and dashed lines are the best-fit relation from Janssens et al. (2017).

2009; Valtchanov et al. 1999; Da Rocha et al. 2005). The abundance of UDGs in HCG 95 is consistent with the overall correlation. However, the clusters Pegasus I cluster and Pegasus II cluster are located below the correlation. We point out that our observations cover only part of the sky area of the two clusters, and the estimated abundance of UDGs is therefore only the lower limit for the abundance of UDGs. The red arrows in Figure 10 denote the lower limits for the two poor clusters. We thus argue that the three galaxy structures in the HCG 95 field follow the same correlation between the abundance of UDGs and halo mass as other galaxy groups and clusters.

4. DISCUSSION

One uncertainty in our analysis is the distance for the selection of UDGs. We identified 89 UDG candidates over a sky area of 4.9 degree² assuming that they are located at the distance of HCG 95, which resides in the galaxy cluster Pegasus II (Rood & Struble 1994). Given that another poor galaxy cluster, Pegasus I, also exists in this field, some candidates may probably be linked with Pegasus I at a distance closer than Pegasus II. Then the actual physical size of these objects would be smaller. The extremely LSB of these candidates makes the measurement of their distance from spectroscopic observations very difficult even with current 10 m class telescopes. In terms of the spatial distribution of bright nearby galaxies with known redshift, the UDG candidates are crudely divided and assigned to the two poor clusters. We estimated that roughly 50 – 60 UDGs are present in the HCG 95 field. This confirms that UDGs

exist in environments with a density that is lower than the density of rich galaxy clusters such as Coma.

The Pegasus I cluster is embedded in the filamentary structures connecting the Pisces-Perseus supercluster (PPS) and the local supercluster (Richter & Huchtmeier 1982; Levy et al. 2007). The velocity dispersion of the Pegasus I cluster is $\sigma \sim 236 \pm 33 \text{ km s}^{-1}$, which is one of the lowest velocities among galaxy clusters (Noonan 1981; Richter & Huchtmeier 1982). We note that there are far fewer UDGs in the Pegasus I region than in the Pegasus II (HCG 95) region. One reason for this is that the Pegasus I cluster is closer, so that the area covered in our observations is smaller, although the angular diameter of the Pegasus I cluster is much larger than the angle of the Pegasus II cluster (Chincarini et al. 1976). However, we cannot deny that the intrinsic abundance of UDGs in the two clusters may differ from each other given their different halo structures. The Pegasus I and Pegasus II clusters both provide a low-density environment. Galaxies in such low-density environments are systematically younger than those in dense environments and their formation timescale is longer (Thomas et al. 2005). The newly formed disk galaxies of the same stellar masses are systematically larger than their analogs at high- z (van der Wel et al. 2014). These suggest that later-type galaxies in low-density environments tend to be formed with larger sizes, compared with those in dense environments. If UDGs are a tail of the high-spin population of galaxies, one could expect that they are more numerous in the low-density environments. On the other hand, UDGs might barely survive in the overdense regions because of strong tidal disruption, leading to a decrease of UDGs.

The detection rate of UDGs in the HCG 95 field is higher than that in the Coma cluster, where 47 UDGs were reported over an area of 8.3 degree² by van Dokkum et al. (2015a). We point out that the depth of survey images affects the detection rate of UDGs. Our images are as deep as those presented by Fliri & Trujillo (2016) and Koda et al. (2015), and deeper than the images by van Dokkum et al. (2015a). Indeed, Koda et al. (2015) claimed that a larger number of UDGs are found in the Coma cluster with deeper imaging data (Yagi et al. 2016). In addition, the detection rate of UDGs is a strong function of the host environment (van der Burg et al. 2016; Román & Trujillo 2017b). As shown in Figure 10, the halo mass of the Coma cluster is higher than the mass of the HCG 95 group, and the abundance of UDGs in HCG 95 is consistent with the halo mass-abundance correlation. Moreover, van Dokkum et al. (2017) pointed out that their estimate of the UDG abundance is incomplete because

the UDGs detected in the SDSS survey were removed from their analysis (e.g., Dragonfly X1).

We find that UDGs in the HCG 95 field span over a wide color range, as shown in Figure 8. The majority of UDGs in our sample have a color comparable to that of red-sequence galaxies of the same stellar masses, consistent with the findings from previous studies (van Dokkum et al. 2015a; van der Burg et al. 2016). Still, a number of UDGs exhibit a color as blue as typical blue-cloud galaxies and HI-selected galaxies. There is no doubt that these blue UDGs are still forming stars. No dependence of color is found on the separation distance from the cluster center. We note that UDGs in the Pegasus II cluster tend to be slightly bluer than those in the Pegasus I cluster. However, this may be due to biases in sample selection as the two subsamples of UDGs show a systematic offset in luminosity.

The presence of blue UDGs indicates that environmental processes quenching star formation in galaxy clusters play a less important role in the Pegasus clusters compared to Coma. Martínez-Delgado et al. (2016) reported DGSAT 1 to be a UDG in PPS and argued that tidal heating effects in combination with ram-pressure stripping remove its gas content and quench star formation in DGSAT 1. Indeed, the lower velocity dispersion of the Pegasus I cluster together with the lack of dense hot intracluster medium (ICM) suggest that ram pressure from hot ICM is no longer a major process for stripping gas in galaxies, and the role of interstellar medium (ISM)-ICM interactions in low-density and low-velocity dispersion environments is a possible explanation (Levy et al. 2007). The proposed mechanisms for the formation of UDGs in dense environments (e.g., rich clusters), including galaxy harassment, ram-pressure stripping and galaxy starvation, do not work for UDGs formed in low-density environments (such as poor clusters and galaxy groups). However, in poor clusters and galaxy groups, the formation of UDGs may be mainly affected by ISM-ICM interactions given their low-velocity dispersions.

Interestingly, we find the UDG H95F in our sample to be a gas-rich galaxy. This UDG has a blue $g - r$ color and strong HI emission detected by VLA. The blue color of H95F suggests that it is dominated by young stellar populations. H95F shows that UDGs partially overlay with HI-selected LSB galaxies. The HI-rich LSB galaxies often have a high spin and low star formation efficiency (Amorisco & Loeb et al. 2016). Our finding reveals that at least part of the UDGs originate from the same parent population as HI-rich LSB galaxies but appear to be extremely low in surface brightness, which might be coupled with the tail of spin at the high end.

This is consistent with the theoretical interpretation by Amorisco & Loeb et al. (2016). In such cases, star formation would not be at a sufficiently high rate to generate the strong outflows that are responsible for the termination of star formation and gas cooling at early time, which is required by the formation mechanism for UDGs seen today (Janowiecki et al. 2015; Trujillo et al. 2017). Feedback from SNe and massive stars driven gas outflows is suggested to inject energy into HI gas, resulting in the expansion of stellar disks and dark matter halos, and the formation of UDGs in the field that mimic LSB galaxies (Di Cintio et al. 2017). We argue that a tidal origin for H95F is unlikely. Although tidal features are clearly seen in the two central galaxies of HCG 95, we do not find apparent tidal structures around H95F from our deep g -band image. It is worth noting that PPS seems to contain about 50% HI-rich galaxies (Richter & Huchtmeier 1982). The Pegasus I cluster (and HCG 95) appears to host more HI gas-rich galaxies. We expect that more UDGs in our sample could be detected with HI in future surveys of higher sensitivities. The gas-rich environment implies that the evolution of galaxies around the Pegasus clusters is still undergoing gas accretion, and the build-up of disks tends to take a longer time compared to other regions. Again, this is consistent with the idea that (at least) some of the UDGs belong to the tail of the high-spin galaxy population formed at a relatively late time.

Owing to the complexity of environmental effects, UDGs may have multiple pathways of formation and evolution. Previous studies suggested that some UDGs could be “failed” galaxies that are overwhelmingly dominated by dark matter (van Dokkum et al. 2015a, 2016, 2017). The high abundance of globular clusters found in one UDG indicates that it may be a failed galaxy with a halo mass similar to the masses of the LMC or M33 (Beasley & Trujillo 2016; Peng & Lim 2016). Other studies revealed that UDGs are part of a dwarf galaxy population (Yozin & Bekki 2015; Amorisco & Loeb et al. 2016; Amorisco et al. 2016; Beasley et al. 2016; Beasley & Trujillo 2016; Di Cintio et al. 2017). Recently, Román & Trujillo (2017b) pointed out that UDGs may be born in the field, further grow in groups, and ultimately fall into galaxy clusters by group accretion, leading to the decrease in UDG density toward dense environments.

In addition, our results show that 26% blue UDGs are detected in our observations. This high abundance of blue UDGs is likely associated with the environment of poor galaxy clusters residing in HI-rich large-scale structures. Taken together, our results indicate that the abundance of blue UDGs tends to be higher in low-

density environments that are still developing, with rich gas available for slowly feeding galaxies to build up LSB disks.

5. SUMMARY

We obtained deep g - and r images of the HCG 95 field with the 1 m CNEOST. Over an area of 4.9 degree², we detected a sample of 89 UDG candidates that are expected to be linked with the two poor galaxy clusters Pegasus I at $z = 0.013$ and Pegasus II at $z = 0.040$. We analyzed the properties of these UDG candidates using available multiwavelength data. We summarize our results as follows:

- (1) There are about 50 – 60 true UDGs with $r_e > 1.5$ kpc and $\mu(g, 0) > 24$ mag arcsec⁻² in the HCG 95 field. These UDGs are most likely associated with the two poor galaxy clusters. This abundance of UDGs is higher than the abundance of UDGs in the field. It becomes clear that UDGs can be found ubiquitously in different environments, but a large diversity of the abundance of UDGs is seen.
- (2) Our UDGs are spread over a wide range in color $g - r$, covering the color regimes of both red-sequence and blue-cloud galaxies. About 23 of them are as blue as blue-cloud galaxies, suggesting that these UDGs are still forming stars. No correlation is found among UDGs between color and separation distance from the density center. Our result indicates that the environmental processes for quenching galaxy star formation appear not to be weak in the volume around HCG 95.
- (3) The morphologies of some UDGs appear to be irregular, the colors of these irregular UDGs are

bluer than regular UDGs, like H95F. This indicates that the irregular UDGs may be connected with loose environments and have a different formation mechanism.

- (4) Our most striking finding is the discovery that UDG H95F is a gas-rich galaxy. This is the first UDG found with solid HI observations by the VLA. Our finding reveals that at least some UDGs may be gas-rich galaxies and overlap the galaxies with low surface brightness galaxies detected in deep HI surveys. This supports the picture that (at least some of the) UDGs belong to the tail of the high-spin galaxy population formed at a relatively late time.

Taken together, our results imply that the abundance of blue UDGs tends to be higher in low-density environments that are still developing, with rich gas available for slowly feeding galaxies. More efforts are needed to determine the environmental complexity and understand the formation of UDGs and their evolutionary pathways.

We are grateful to the referee for the valuable comments and suggestions that have improved our manuscript. This work is supported by the National Basic Research Program of China (973 Program 2013CB834900), the National Natural Science Foundation of China through grant U1331110, and the Chinese Academy of Sciences (CAS), through a grant to the CAS South America Center for Astronomy (CASSACA) in Santiago, Chile.

REFERENCES

- Abell, G. O., Corwin, H. G., Jr., & Olowin, R. P. 1989, *ApJS*, 70, 1
- Abraham, R. G., & van Dokkum, P. G. 2014, *PASP*, 126, 55
- Amorisco, N. C. & Loeb, A., 2016, *MNRAS*, 459, L51
- Amorisco, N. C., Monachesi, A., & White, S. D. M. 2016, *arXiv:1610.01595*
- Barnes, D. G., Webster, R. L., Schmidt, R. W., & Hughes, A. 1999, *MNRAS*, 309, 641
- Beasley, M. A., Romanowsky, A. J., Pota, V., et al. 2016, *ApJL*, 819, L20
- Beasley, M. A., & Trujillo, I. 2016, *ApJ*, 830, 23
- Bell, E. F., McIntosh, D. H., Katz, N., & Weinberg, M. D. 2003, *ApJS*, 149, 289
- Bellazzini, M., Belokurov, V., Magrini, L., et al. 2017, *MNRAS*, 467, 3751
- Bertin, E., & Arnouts, S. 1996, *A&AS*, 117, 393
- Bertin, E., Mellier, Y., Radovich, M., et al. 2002, in *ASP Conf. Ser. 281, Astronomical Data Analysis Software and Systems XI*, ed. D. A. Bohlender, D. Durand, & T. H. Handley (San Francisco, CA: ASP), 228

- Bertin, E. 2006, in ASP Conf. Ser. 351, *Astronomical Data Analysis Software and Systems XV*, ed. C. Gabriel, C. Arviset, D. Ponz, & E. Solano (San Francisco, CA: ASP), 112
- Blanton, M. R., Eisenstein, D., Hogg, D. W., & Zehavi, I. 2006, *ApJ*, 645, 977
- Blum, R. D., Burleigh, K., Dey, A., et al. 2016, *AAS Meeting*, 228, 317.01
- Bothun, G. D., Impey, C. D., & Malin, D. F. 1991, *ApJ*, 376, 404
- Bouché, N., Carfantan, H., Schroetter, I., Michel-Dansac, L., & Contini, T. 2015, *AJ*, 150, 92
- Brodie, J. P., Romanowsky, A. J., Strader, J., & Forbes, D. A. 2011, *AJ*, 142, 199
- Bruzual, G., & Charlot, S. 2003, *MNRAS*, 344, 1000
- Canizares, C. R., Donahue, M. E., Trinchieri, G., Stewart, G. C., & McGlynn, T. A. 1986, *ApJ*, 304, 312
- Ceccarelli, L., Herrera-Camus, R., Lambas, D. G., Galaz, G., & Padilla, N. D. 2012, *MNRAS*, 426, L6
- Chincarini, G., & Rood, H. J. 1976, *PASP*, 88, 388
- Di Cintio, A., Brook, C. B., Dutton, A. A., et al. 2017, *MNRAS*, 466, L1
- Da Rocha, C. & Mendes de Oliveira, C. 2005, *MNRAS*, 364, 1069
- Falco, E. E., Kurtz, M. J., Geller, M. J., et al. 1999, *PASP*, 111, 438
- Fliri, J., & Trujillo, I. 2016, *MNRAS*, 456, 1359
- Freyhammer, L. M., Andersen, M. I., Arentoft, T., Sterken, C., & Nørregaard, P. 2001, *Experimental Astronomy*, 12, 147
- Fukugita, M., Ichikawa, T., Gunn, J. E., et al. 1996, *AJ*, 111, 1748
- Gavazzi, G., Donati, A., Cucciati, O., et al. 2005, *A&A*, 430, 411
- Geller, M. J., Diaferio, A., Kurtz, M. J., Dell'Antonio, I. P., & Fabricant, D. G. 2012, *AJ*, 143, 102
- Giovanelli, R., Haynes, M. P., Kent, B. R., et al. 2005, *AJ*, 130, 2598
- Girardi, M., Giuricin, G., Mardirossian, F., Mezzetti, M., & Boschini, W. 1998, *ApJ*, 505, 74
- Graham, A. W., & Driver, S. P. 2005, *PASA*, 22, 118
- Haynes, M. P., Giovanelli, R., Martin, A. M., et al. 2011, *AJ*, 142, 170
- Hickson, P., Mendes de Oliveira, C., Huchra, J. P., & Palumbo, G. G. 1992, *ApJ*, 399, 353
- Huchtmeier, W. K., Verdes-Montenegro, L., Yun, M., del Olmo, A., & Perea, J. 2000, in *IAU Colloq. 174: Small Galaxy Groups*, ed. M.J. Valtonen & C. Flynn (San Francisco, CA: ASP), 154
- Iglesias-Páramo, J., & Vílchez, J. M. 1997, *ApJL*, 489, L13
- Iglesias-Páramo, J., & Vílchez, J. M. 1998, *AJ*, 115, 1791
- Iglesias-Páramo, J., & Vílchez, J. M. 2001, *ApJ*, 550, 204
- Impey, C., Bothun, G., & Malin, D. 1988, *ApJ*, 330, 634
- Impey, C. D., Sprayberry, D., Irwin, M. J., & Bothun, G. D. 1996, *ApJS*, 105, 209
- Impey, C., & Bothun, G. 1997, *ARA&A*, 35, 267
- Impey, C., Burkholder, V., & Sprayberry, D. 2001, *AJ*, 122, 2341
- Janowiecki, S., Leisman, L., Józsa, G., et al. 2015, *ApJ*, 801, 96
- Janssens, S., Abraham, R., Brodie, J., et al. 2017, *ApJL*, 839, L17
- Koch, A., Black, C. S., Rich, R. M., et al. 2017, *Astronomische Nachrichten*, 338, 503
- Koda, J., Yagi, M., Yamanoi, H., & Komiyama, Y. 2015, *ApJL*, 807, L2
- Leisman, L., Haynes, M. P., Janowiecki, S., et al. 2017, *ApJ*, 842, 133
- Levy, L., Rose, J. A., van Gorkom, J. H., & Chaboyer, B. 2007, *AJ*, 133, 1104
- Martínez-Delgado, D., Läsker, R., Sharina, M., et al. 2016, *AJ*, 151, 96
- Merritt, A., van Dokkum, P., Danieli, S., et al. 2016, *ApJ*, 833, 168
- Mihos, J. C., Durrell, P. R., Ferrarese, L., et al. 2015, *ApJL*, 809, L21
- Muñoz, R. P., Eigenthaler, P., Puzia, T. H., et al. 2015, *ApJL*, 813, L15
- Noonan, T. W. 1981, *ApJS*, 45, 613
- O'Neil, K., Bothun, G. D., & Cornell, M. E. 1997, *AJ*, 113, 1212
- Ordenes-Briceño, Y., Taylor, M. A., Puzia, T. H., et al. 2016, *MNRAS*, 463, 1284
- Peng, C. Y., Ho, L. C., Impey, C. D., & Rix, H.-W. 2002, *AJ*, 124, 266
- Peng, E. W., & Lim, S. 2016, *ApJL*, 822, L31
- Ponman, T. J., Bourner, P. D. J., Ebeling, H., et al. 1996, *MNRAS*, 283, 690
- Randall, S. W., Jones, C., Kraft, R., Forman, W. R., & O'Sullivan, E. 2009, *ApJ*, 696, 1431
- Richter, O.-G., & Huchtmeier, W. K. 1982, *A&A*, 109, 155
- Rodrigue, M., Schultz, A., Thompson, J., et al. 1995, *AJ*, 109, 2362
- Román, J., & Trujillo, I. 2017, *MNRAS*, 468, 703
- Román, J., & Trujillo, I. 2017, *MNRAS*, 468, 4039
- Rood, H. J., & Struble, M. F. 1994, *PASP*, 106, 413
- Smith Castelli, A. V., Faifer, F. R., & Escudero, C. G. 2016, *A&A*, 596, A23
- Taylor, E. N., Hopkins, A. M., Baldry, I. K., et al. 2011, *MNRAS*, 418, 1587

- Teimoorinia, H., Ellison, S. L., & Patton, D. R. 2017, MNRAS, 464, 3796
- Thomas, D., Maraston, C., Bender, R., & Mendes de Oliveira, C. 2005, ApJ, 621, 673
- Trujillo, I., Roman, J., Filho, M., & Sánchez Almeida, J. 2017, ApJ, 836, 191
- Valtchanov, I., Kalinkov, M., & Kuneva, I. 1999, in Proc. Int. Conf. on Numerical Astrophysics, ed. S.M. Miyama, K. Tomisaka, & T. Hanawa (Boston, MA: Kluwer Academic), 59
- van der Burg, R. F. J., Muzzin, A., & Hoekstra, H. 2016, A&A, 590, A20
- van der Wel, A., Chang, Y.-Y., Bell, E. F., et al. 2014, ApJL, 792, L6
- van Dokkum, P., Abraham, R., Brodie, J., et al. 2016, ApJL, 828, L6
- van Dokkum, P., Abraham, R., Romanowsky, A. J., et al. 2017, ApJL, 844, L11
- van Dokkum, P. G., Abraham, R., Merritt, A., et al. 2015, ApJL, 798, L45
- van Dokkum, P. G., Romanowsky, A. J., Abraham, R., et al. 2015, ApJL, 804, L26
- Verdes-Montenegro, L., Yun, M., Perea, J., & del Olmo, A. 1997, in ASP Conf. 117, Dark and Visible Matter in Galaxies and Cosmological Implications, ed. M. Persic & P. Salucci (San Francisco, CA: ASP), 530
- Yagi, M., Koda, J., Komiyama, Y., & Yamanoi, H. 2016, ApJS, 225, 11
- Yozin, C., & Bekki, K. 2015, MNRAS, 452, 937
- Zhang, H.-H., Liu, X.-W., Yuan, H.-B., et al. 2013, Research in Astronomy and Astrophysics, 13, 490
- Zhang, H.-H., Liu, X.-W., Yuan, H.-B., et al. 2014, Research in Astronomy and Astrophysics, 14, 456
- Zhong, G. H., Liang, Y. C., Liu, F. S., et al. 2008, MNRAS, 391, 986

APPENDIX

Here we present additional technical details of our data analysis.

Figure A.1 shows the PSF FWHM map for the g - and r -band mosaicked science images. It is shown that the PSF varies over our wide-field region in the sense that it increases from the center to the edges. We use point sources to fit a third-order polynomial and build up the maps. The typical PSF FWHM is $4''$ and $3''$ at the center region of the g - and r -band mosaicked image, respectively.

Figure A.2 shows a comparison of our g - and r -band photometry with the SDSS for bright stars ($14 < g < 18$ mag) in different annular regions of the FOV. We divide our area into four annular regions, including $R < 0^\circ 37$, $0^\circ 37 < R < 0^\circ 74$, $0^\circ 74 < R < 1^\circ 11$ and $1^\circ 11 < R < 1^\circ 45$. Our photometry is in agreement with the photometric magnitude of the SDSS.

In Figure A.3 we compare the half-light radius of bright galaxies ($15 < g < 19$ mag) in the different annular regions from the center to the edges. We also divide our area into four annular regions, including $R < 0^\circ 37$, $0^\circ 37 < R < 0^\circ 74$, $0^\circ 74 < R < 1^\circ 11$ and $1^\circ 11 < R < 1^\circ 45$. We use the SDSS half-light radius of bright galaxies ($15 < g < 19$ mag) to calibrate our measurements. The top four panels of Figure A.3 show the comparison of the observed half-light radius without PSF correction. It is clearly seen that the PSF effect on the measurement of the half-light radius becomes larger for more compact objects with $r_{\text{SDSS}} < 3''$. Some outliers are mainly affected by the contamination of scattered light and the asterism from saturation stars. The bottom panels show the measurements of the half-light radius corrected for PSF. The median ratio of half-light radius between the SDSS and Xuyi is 0.85, the dispersion is 0.16. This discrepancy is likely caused by the systematic effects related to pixel scale and instrumental effects. The size of the PSF (R_{psf}) is about $2''.7 - 3''.5$ in the g -band mosaicked image. We therefore use the PSF-corrected half-light radius to calculate the central surface brightness for selecting UDGs (see Section 3), although the measurement errors are relatively large.

Table A.1 lists the catalog of our selected UDGs in the HCG 95 field. We assume that 89 extremely LSB galaxies are spatially separated members of the clusters Pegasus I and Pegasus II cluster. Finally, we pick out 32 very LSB galaxies (with a size is smaller than 1.5 kpc), 12 plausible UDGs, and 45 UDGs at the distance of the clusters Pegasus I and Pegasus II, respectively. The properties of these candidates are shown in Table A.1. Fortunately, 84 of the 89 very LSB galaxies are detected in deep z' -band images by DECaLS. The magnitudes and half-light radii of the 84 candidates are listed in Table A.1. We use brackets to represent the lower size limits because some UDGs have very low signal-to-noise at z' -band image.

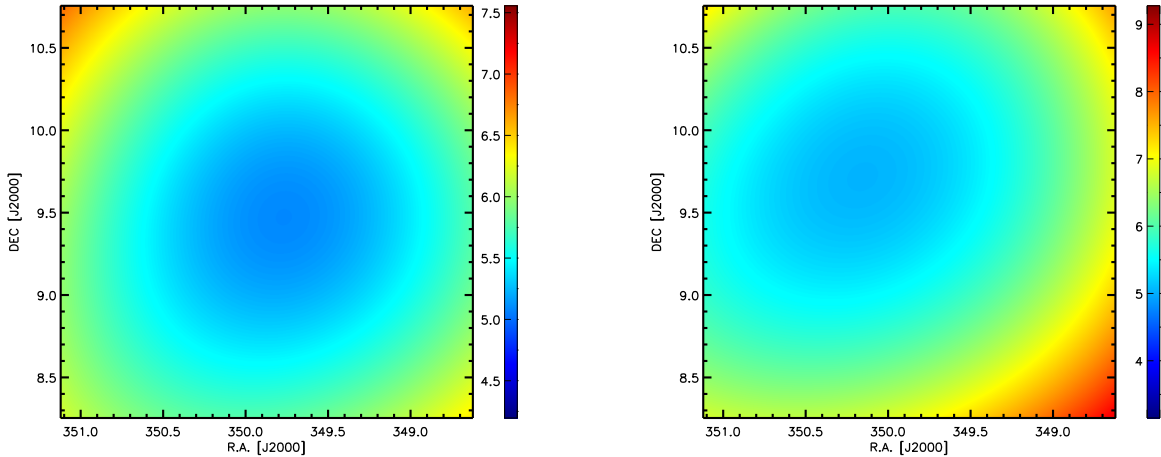


Figure A.1. The PSF FWHM map for the g - and r -band mosaicked images. The PSF varies over our wide-field region and it increases from the center to the edges. Left: the PSF FWHM map for the g -band image in the $2^\circ 5 \times 2^\circ 5$ region. Right: the PSF FWHM map for r -band image in the $2^\circ 5 \times 2^\circ 5$ region.

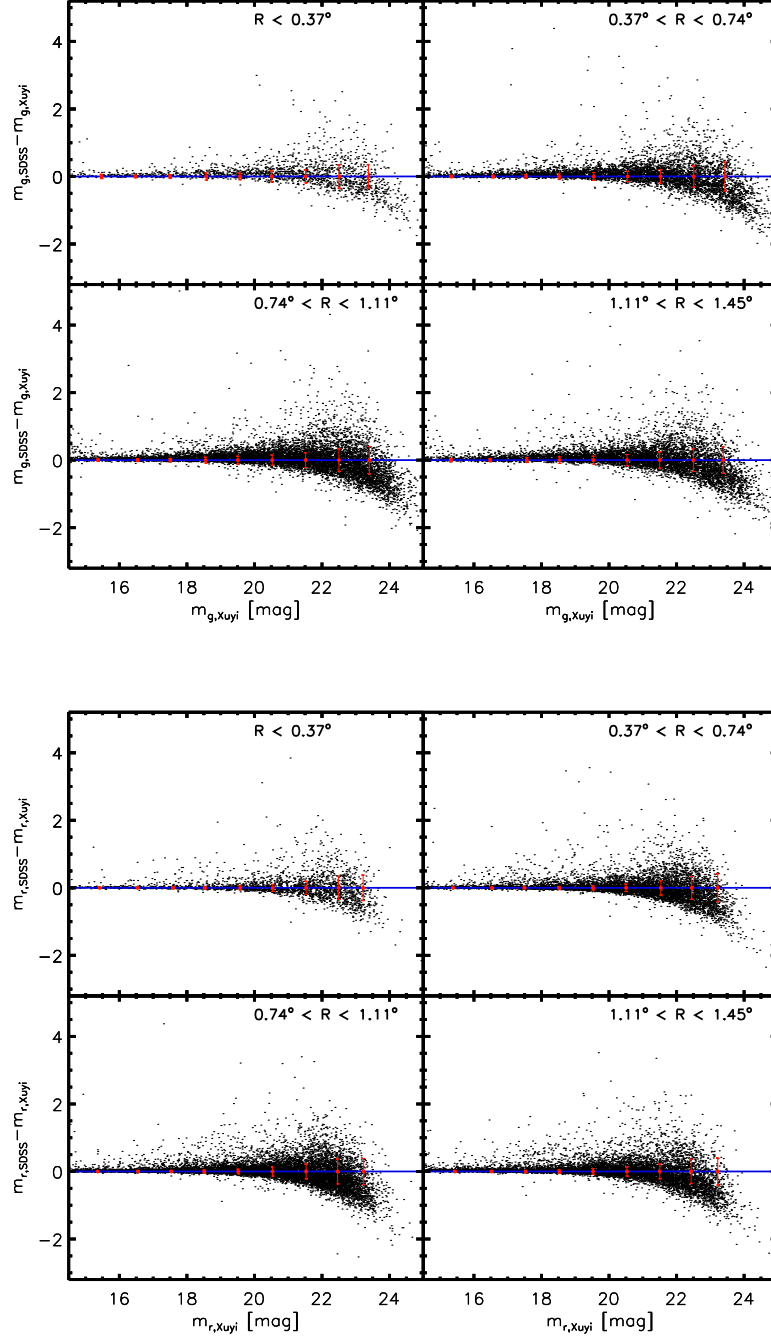


Figure A.2. Comparison of our g - and r -band photometry with the SDSS for bright stars ($14 < g < 18$ mag) in different annular regions. The dispersion of faint stars is larger than bright stars. Our photometry is in agreement with the photometric magnitude of the SDSS. The top panels denote the g -band photometry with the SDSS for bright stars, the bottom panels show the r -band photometry with the SDSS for bright stars.

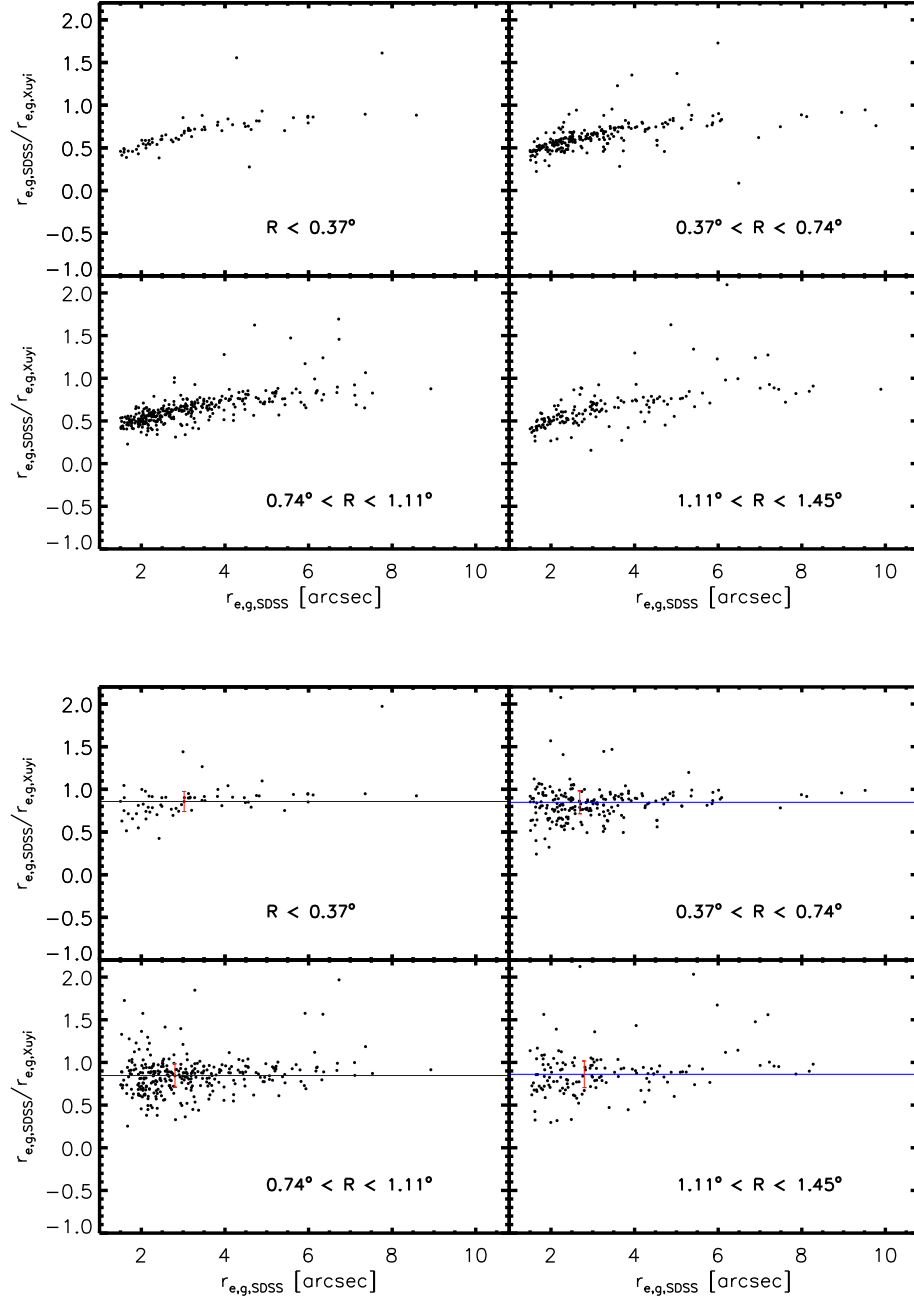


Figure A.3. Comparison of the half-light radius of bright galaxies ($15 < g < 19$ mag) in the different regions from the center to the edges. Upper panels: comparison of the observed half-light radius without PSF correction. Bottom panels: measurements of the half-light radius corrected for PSF.

Table A.1. Properties of UDGs in the HCG 95 field

ID	R.A. (J2000.0)	Decl. (J2000.0)	$\mu(g, 0)$ (mag arcsec ⁻²)	r_e (kpc)	M_g (mag)	b/a	$g - r$ (mag)	DECaLs(z') (mag)	DECaLs(r_e, z') (kpc)
PegI-LSBG01	23:19:03.6	8:23:15	26.36	1.38	-12.29	0.90	0.49	21.24	[0.49]
PegI-LSBG02	23:18:35.6	8:23:39	24.58	0.97	-13.61	0.94	0.65	18.93	0.78
PegI-LSBG03	23:19:43.8	8:26:23	24.00	0.93	-14.03	0.80	0.48	18.57	0.78
PegI-LSBG04	23:17:49.9	8:28:05	25.13	1.32	-13.60	0.82	0.67	19.18	0.80
PegI-LSBG05	23:20:46.9	8:28:29	24.88	1.32	-13.69	0.72	0.75	19.46	0.72
PegI-LSBG06	23:18:28.1	8:28:58	26.45	1.33	-12.46	0.97	0.53	21.77	[0.36]
PegI-LSBG07	23:19:11.9	8:33:32	25.09	0.91	-12.78	0.79	0.64	20.39	[0.50]
PegI-LSBG08	23:20:37.4	8:35:26	24.29	1.21	-13.80	0.55	0.53	19.04	0.64
PegI-LSBG09	23:21:45.5	8:37:41	25.02	0.86	-12.25	0.51	0.74	20.49	[0.32]
PegI-LSBG10	23:20:13.1	8:39:31	24.58	1.24	-13.59	0.56	0.72	18.97	0.71
PegI-LSBG11	23:21:10.6	8:39:45	24.10	1.06	-13.52	0.46	0.60	19.11	0.63
PegI-LSBG12	23:22:08.4	8:41:60	24.27	0.56	-12.26	0.61	0.39	21.22	[0.27]
PegI-LSBG13	23:18:22.2	8:42:53	25.41	0.65	-11.73	0.81	0.67	21.89	[0.19]
PegI-LSBG14	23:19:47.0	8:42:33	24.62	1.01	-13.55	0.84	0.67	19.00	0.74
PegI-LSBG15	23:21:22.9	8:43:11	26.32	1.05	-11.99	0.89	0.96	22.05	[0.19]
PegI-LSBG16	23:22:55.7	8:44:46	25.74	1.07	-11.99	0.51	0.41	21.52	[0.25]
PegI-LSBG17	23:22:09.1	8:48:49	25.56	1.01	-12.01	0.49	0.93	21.15	[0.36]
PegI-LSBG18	23:23:24.5	8:50:49	25.31	0.86	-12.21	0.60	0.57	21.34	[0.28]
PegI-LSBG19	23:20:13.5	8:54:31	24.25	0.95	-13.66	0.53	0.75	18.94	0.71
PegI-LSBG20	23:22:58.0	8:54:43	24.00	0.89	-13.88	0.78	0.64	18.79	0.69
PegI-LSBG21	23:22:10.7	8:56:52	25.83	1.00	-12.04	0.65	0.82	21.23	[0.27]
PegI-LSBG22	23:23:59.3	8:57:03	25.76	0.95	-12.04	0.68	0.89	20.91	[0.23]
PegI-LSBG23	23:23:00.8	8:59:56	24.92	1.01	-13.11	0.75	0.67	19.87	0.74
PegI-LSBG24	23:21:36.2	9:03:41	24.14	0.88	-13.47	0.66	0.76	19.60	0.61
PegI-LSBG25	23:22:28.3	9:04:19	24.05	0.94	-13.74	0.54	0.65	19.35	0.55
PegI-LSBG26	23:20:41.8	9:09:02	24.55	0.97	-12.92	0.50	0.75	20.37	[0.45]
PegI-LSBG27	23:24:25.3	9:12:22	24.02	0.98	-14.14	0.88	0.34	19.00	0.74

Table A.1 continued

Table A.1 (continued)

ID	R.A.	Decl.	$\mu(g, 0)$	r_e	M_g	b/a	$g - r$	DECaLs(z')	DECaLs(r_e, z')
	(J2000.0)	(J2000.0)	(mag arcsec $^{-2}$)	(kpc)	(mag)		(mag)	(mag)	(kpc)
PegI-LSBG28	23:22:44.7	9:19:52	24.17	0.82	-13.64	0.92	0.27	19.71	0.51
PegI-LSBG29	23:21:39.5	9:21:36	24.33	1.04	-13.92	0.86	0.42	18.98	0.75
PegI-LSBG30	23:23:36.9	9:37:48	25.84	0.76	-11.62	0.80	0.38	21.61	[0.28]
PegI-LSBG31	23:23:46.8	9:43:59	24.11	0.94	-13.24	0.46	0.72	19.55	0.46
PegI-LSBG32	23:24:04.5	9:44:43	25.20	1.15	-13.32	0.90	0.41	20.31	[0.43]
PegI-UDG01	23:20:04.9	8:21:29	24.43	1.65	-14.31	0.53	0.70	18.21	0.88
PegI-UDG02	23:21:07.3	8:23:44	25.02	1.93	-14.11	0.56	0.69	18.93	0.89
PegI-UDG03	23:21:57.3	8:26:27	25.51	2.75	-14.85	0.85	0.69	20.15	[0.49]
PegI-UDG04	23:21:34.4	8:28:39	25.28	2.49	-14.66	0.71	0.83	18.72	1.16
PegI-UDG05	23:21:34.6	8:29:26	24.67	2.44	-15.29	0.77	0.76	17.40	1.68
PegI-UDG06	23:20:20.8	8:33:05	24.38	1.61	-14.80	0.85	0.71	17.99	0.97
PegI-UDG07	23:19:57.8	8:33:19	24.47	1.55	-14.39	0.68	0.57	18.64	0.80
PegI-UDG08	23:18:52.5	8:40:47	24.08	1.88	-14.96	0.55	0.58	17.93	1.17
PegI-UDG09	23:19:39.5	8:42:32	25.45	1.51	-13.13	0.69	0.80	20.40	[0.61]
PegI-UDG10	23:21:01.4	8:50:02	26.19	1.86	-13.20	0.75	0.63	21.09	[0.53]
PegI-UDG11	23:21:41.1	9:07:12	24.33	1.99	-15.21	0.77	0.52	17.51	1.51
PegI-UDG12	23:23:59.5	9:51:18	24.55	2.33	-15.19	0.67	0.58	18.36	1.02
PegII-UDG01	23:17:07.0	8:39:06	25.88	2.92	-14.27	0.59	0.23	20.25	[1.20]
PegII-UDG02	23:16:13.6	8:44:13	24.31	1.70	-15.19	0.94	0.73	20.12	[1.44]
PegII-UDG03	23:16:04.3	8:48:15	24.57	1.93	-15.04	0.79	0.15	20.93	[0.91]
PegII-UDG04	23:16:08.6	8:53:56	25.29	3.44	-15.28	0.66	0.63	19.88	1.92
PegII-UDG05	23:18:09.2	8:53:30	24.02	2.06	-15.34	0.43	0.58	20.42	[1.11]
PegII-UDG06	23:17:20.7	8:59:08	25.18	2.26	-14.67	0.78	0.40	21.24	[0.66]
PegII-UDG07	23:15:17.5	8:59:35	24.00	3.14	-16.29	0.56	0.40	19.14	1.90
PegII-UDG08	23:16:18.1	9:01:14	24.07	4.20	-16.94	0.60	0.47	18.85	2.47
PegII-UDG09	23:14:57.6	9:04:59	25.57	4.23	-15.47	0.54	0.74	20.40	[1.11]
PegII-UDG10	23:20:11.7	9:18:27	24.0	3.64	-16.95	0.76	0.40	18.50	2.59
PegII-UDG11	23:15:28.6	9:18:45	24.83	4.40	-16.38	0.71	0.57
PegII-UDG12	23:18:02.2	9:20:18	24.01	1.61	-15.06	0.71	0.57	20.63	[1.09]

Table A.1 continued

Table A.1 (continued)

ID	R.A.	Decl.	$\mu(g, 0)$	r_e	M_g	b/a	$g - r$	DECaLs(z')	DECaLs(r_e, z')
	(J2000.0)	(J2000.0)	(mag arcsec ⁻²)	(kpc)	(mag)		(mag)	(mag)	(kpc)
PegII-UDG13	23:18:56.0	9:20:18	25.08	2.97	-15.22	0.65	0.37	21.09	[1.49]
PegII-UDG14	23:18:58.2	9:21:41	24.0	2.49	-16.20	0.78	0.70	19.01	1.99
PegII-UDG15	23:18:10.2	9:27:13	24.09	3.33	-16.23	0.54	0.72	19.07	1.40
PegII-UDG16	23:20:36.8	9:30:02	25.04	2.36	-14.92	0.75	0.69	20.15	[1.56]
PegII-UDG17	23:17:44.9	9:29:38	24.00	3.79	-17.07	0.72	0.48	18.44	3.05
PegII-UDG18	23:17:34.4	9:30:16	25.36	2.74	-15.02	0.82	0.40	20.92	[1.42]
PegII-UDG19	23:19:21.5	9:30:14	24.12	2.94	-16.27	0.88	0.40	19.02	2.26
PegII-UDG20	23:18:32.5	9:31:54	24.04	3.34	-16.57	0.58	0.56	19.63	1.58
PegII-UDG21	23:20:22.6	9:32:58	24.48	2.28	-15.14	0.58	0.44	20.40	[1.60]
PegII-UDG22	23:17:38.8	9:33:26	24.00	2.31	-15.90	0.74	0.55	19.27	2.21
PegII-UDG23 ^a	23:19:29.0	9:33:31	24.05	3.41	-16.69	0.74	0.28	20.10	[1.25]
PegII-UDG24	23:18:10.1	9:35:14	24.53	2.85	-15.84	0.76	0.66	19.41	1.80
PegII-UDG25	23:22:19.5	9:37:07	24.43	5.66	-17.15	0.52	0.36	18.65	3.23
PegII-UDG26	23:14:41.4	9:39:07	24.15	1.74	-14.82	0.55	0.74	21.57	[0.85]
PegII-UDG27	23:14:50.4	9:39:02	25.32	3.36	-14.82	0.60	0.68	22.22	[0.73]
PegII-UDG28	23:20:36.5	9:40:16	25.56	2.98	-14.53	0.53	0.83
PegII-UDG29	23:21:31.6	9:42:09	24.32	4.11	-16.56	0.58	0.70	19.06	1.84
PegII-UDG30	23:21:02.0	9:45:17	24.34	2.97	-15.86	0.58	0.76	20.35	[1.58]
PegII-UDG31	23:18:04.1	9:50:29	24.38	3.15	-16.39	0.89	0.56	19.28	1.87
PegII-UDG32	23:17:45.4	9:50:43	24.22	1.73	-14.86	0.65	0.99	21.18	[1.10]
PegII-UDG33	23:17:40.1	9:50:51	24.16	2.87	-16.12	0.68	0.80	19.22	1.79
PegII-UDG34	23:17:27.7	9:52:12	24.13	2.67	-15.92	0.64	0.52	19.69	1.77
PegII-UDG35	23:17:08.8	9:53:55	24.00	3.50	-17.11	0.98	0.58
PegII-UDG36	23:22:24.7	9:54:15	24.80	4.04	-16.28	0.84	0.59	19.24	1.66
PegII-UDG37	23:22:08.2	9:54:47	24.20	4.11	-17.14	0.89	0.39	18.97	2.29
PegII-UDG38	23:18:56.3	9:55:18	24.04	3.37	-16.37	0.55	0.46	19.20	1.92
PegII-UDG39	23:23:59.5	10:11:01	24.07	3.30	-16.49	0.67	0.47	18.79	1.95
PegII-UDG40	23:20:10.9	10:16:12	25.22	3.85	-15.68	0.67	0.53	20.07	[1.42]
PegII-UDG41	23:21:35.6	10:17:56	24.50	3.86	-16.22	0.56	0.62

Table A.1 continued

Table A.1 (*continued*)

ID	R.A. (J2000.0)	Decl. (J2000.0)	$\mu(g, 0)$ (mag arcsec ⁻²)	r_e (kpc)	M_g (mag)	b/a	$g - r$ (mag)	DECaLs(z') (mag)	DECaLs(r_e, z') (kpc)
PegII-UDG42	23:22:00.3	10:21:12	24.38	2.73	-16.16	0.96	0.46	19.00	2.02
PegII-UDG43	23:20:28.5	10:28:12	24.44	2.94	-15.90	0.69	0.64	19.81	1.65
PegII-UDG44	23:18:10.6	10:33:50	25.01	3.04	-15.37	0.66	0.60
PegII-UDG45	23:18:43.5	10:35:40	24.14	2.06	-15.38	0.65	0.39	20.32	[1.56]

^aH95F = PegII-UDG25